Targeted transplantation of engineered mitochondrial compound promotes functional recovery after spinal cord injury by enhancing macrophage phagocytosis

Jiaqi Xu [a,b,c,1], Chaoran Shi [a,b,c,1], Feifei Yuan [a,b,c], Yinghe Ding [a,b,c], Yong Xie [a,b,c], Yudong Liu [a,b,c], Fengzhang Zhu [a,b,c], Hongbin Lu [b,c,d], Chunyue Duan [a,b,c], Jianzhong Hu [a,b,c,**], Liyuan Jiang [a,b,c,*]

[a] Department of Spine Surgery and Orthopaedics, Xiangya Hospital, Central South University, Changsha, 410008, Hunan Province, China
[b] Key Laboratory of Organ Injury, Aging and Regenerative Medicine of Hunan Province, Changsha, 410008, Hunan Province, China
[c] National Clinical Research Center for Geriatric Disorders, Xiangya Hospital, Central South University, Changsha, 410008, Hunan Province, China
[d] Department of Sports Medicine, Xiangya Hospital, Central South University, Changsha, 410008, Hunan Province, China

ARTICLE INFO

ABSTRACT

Mitochondria are crucial in sustaining and orchestrating cellular functions. Capitalizing on this, we explored mitochondrial transplantation as an innovative therapeutic strategy for acute spinal cord injury (SCI). In our study, we developed an engineered mitochondrial compound tailored to target macrophages within the SCI region. Sourced from IL-10-induced Mertk^{hi} bone marrow-derived macrophages, we conjugated a peptide sequence, cations-cysteine-alanine-glutamine-lysine (CAQK), with the mitochondria, optimizing its targeting affinity for the injury site. Our data demonstrated that these compounds significantly enhanced macrophage phagocytosis of myelin debris, curtailed lipid buildup, ameliorated mitochondrial dysfunction, and attenuated pro-inflammatory profiles in macrophages, both in vitro and *in vivo*. The intravenously delivered mitochondrial compounds targeted the SCI epicenter, with macrophages being the primary recipients. Critically, they promoted tissue regeneration and bolstered functional recovery in SCI mice. This study heralds a transformative approach to mitochondrial transplantation in SCI, spotlighting the modulation of macrophage activity, phagocytosis, and phenotype.

1. Introduction

Traumatic spinal cord injury (SCI) is a devastating event that damages the central nervous system, often leading to paralysis, disability, and in the worst cases, death [1]. Over the past three decades, the incidence and burden of SCI have markedly increased worldwide, with an estimated 0.9 million new cases, 20.6 million prevalent cases, and 6.2 million individuals living with disabilities globally [2,3]. Despite ongoing research on various neuro-regenerative strategies, such as cell transplantation [4], exosome-based approaches [5], and bioengineered biomaterials [6], there is still a need for effective therapies to promote efficient recovery from SCI. During the acute phase of SCI, the disruption of microvascular triggers a cascade of environmental changes. Including inflammatory cell infiltration, cytotoxic product release, and free radical generation [1,7]. The various cells in the epicenter of injury undergo mitochondrial dysfunction in an ischemic and hypoxic environment [8]. Hence, restoring cellular energetics by modulating mitochondrial response has emerged as a promising approach for promoting recovery after SCI [9]. However, pharmacological interventions that can enhance mitochondrial energy production and prevent the loss of physiological mitochondrial function remain to be developed.

Mitochondrial transplantation is a rapidly growing approach in mitochondrial medicine, which involves the transfer of healthy mitochondria from an exogenous source into damaged tissues to rescue cells

---

or tissues [10]. This technique is based on the endosymbiotic theory, which suggests that eukaryotic cells may have engulfed free-living aerobic bacteria that eventually evolved into mitochondria. This symbiosis resulted in increased energy efficiency and improved survival prospects for the host cells [11]. Mitochondria can also be transferred intercellularly under physiological conditions, indicating their survival ability in recipient cells and paving the way for mitochondrial transplantation therapy [12]. Recently, mitochondrial transplantation has shown promise in the treatment of ischemic and hypoxic diseases, including cardiovascular disorders, cancer, and neurological diseases [13–15]. Several studies have attempted to use mitochondrial transplantation for the treatment of spinal cord injuries in rats. However, these efforts did not thoroughly investigate the recipient cells of the transplanted mitochondria [16–19]. Gollihue et al., however, revealed that the transplanted mitochondria were absent in neurons [17]. Furthermore, in situ injection of mitochondria may cause additional damage to the fragile neural tissue [16,17], while tail vein injection of mitochondria lacks targeting specificity [18]. The effects of transplanted mitochondria on cells and the microenvironment within the injured area are still largely unknown. Therefore, the development of refined mitochondrial delivery techniques and the comprehensive investigation of mitochondrial recipient cells are crucial for the success of this promising therapeutic approach.

Macrophages play a crucial role in neuroinflammation and tissue repair as they identify, engulf, and degrade of pathogens, apoptotic cells, and tissue debris [20]. Myelin debris accumulates in large quantities after traumatic SCI and becomes a crucial hindrance to neural regeneration [21]. Macrophages promote remyelination and axonal regeneration by removing the inhibitory myelin debris [20]. However, excessive phagocytosis can lead to lipid accumulation and dysregulated intracellular lipid homeostasis, producing pro-inflammatory and foamy macrophages [22–24]. This leads to impaired macrophage function and the persistence of M1 macrophages, which further hinder the prompt clearance of myelin debris and neural tissue regeneration [25]. Mitochondrial and metabolic dysfunction are closely related to the phenotypic switch of macrophages, with pro-inflammatory macrophages exhibiting elevated glycolysis and decreased mitochondrial oxidative phosphorylation (OXPHOS) efficiency. Efficient mitochondrial respiration and OXPHOS are essential for macrophages to adopt reparative/anti-inflammatory phenotypes and functions [26,27]. Moreover, the energetic metabolic pathway is critical for the phagocytosis and lipid-handling activity of macrophages [28,29]. However, it remains unclear whether regulating macrophage mitochondrial function can effectively promote rehabilitation after SCI. To date, no studies have examined mitochondrial transplantation targeted specifically to macrophages. Thus, transplanting highly functional mitochondria has the potential to enhance the phagocytic capacity of macrophages and facilitate their transition towards a reparative phenotype following SCI.

In this study, we utilized interleukin-10 (IL-10)-induced mer tyrosine kinase high expression (Mertk^{hi}) m2c macrophages as energetic sources for mitochondria transplantation and constructed an engineered mitochondrial - triphenylphosphonium cations – (cysteine-alanine-glutamine-lysine) (Mito-Tpp-CAQK) compound to evaluate its therapeutic effect on SCI in mice. The IL-10-induced Mertk^{hi} macrophages showed excellent mitochondrial quality and function [30,31]. Moreover, CAQK is a peptide that can effectively target proteoglycan compounds in the injured epicenter after SCI [32,33]. We comprehensively evaluated the intravenously administered mitochondrial compound's effectiveness in targeting the injury site, as well as its impact on macrophage phagocytosis and phenotypes. Our findings may provide a promising approach for the treatment of SCI, which warrants further investigation and validation.

2. Materials & methods

2.1. Bioinformatic analysis of the single-cell transcriptomic dataset

The single-cell RNA sequencing data and annotation information for a mouse spinal cord injury with contusion were retrieved from the GEO database (https://www.ncbi.nlm.nih.gov/geo/, accession number GSE162610). Briefly, CellRanger (v2-4) was utilized to convert the Illumina output into gene barcode count matrices, which were subsequently subjected to additional analysis. Data processing and the expression levels of Mertk in cell clusters were performed using the R package "Seurat" [34].

2.2. Mouse bone marrow-derived macrophage preparation and culture

C57BL/6 mice (8 weeks old, weight 20–25 g) were selected and euthanized randomly after a week of adjustable feeding. They were sterilized by being immersed in a 75% alcohol solution for 5–6 min and fixed onto a surgical plate within an ultra-clean environment. A skin incision was made in the groin area, the lower limb muscles were then separated, and the femur and tibia were carefully exposed and removed intact. The femur and tibia were carefully separated along the joint, and residual muscle tissue was meticulously removed. Once both sides of the epiphysis were separated, the bone marrow cells were flushed out using a 20 mL syringe filled with culture medium. These cells were then gently blown repeatedly with a dropper, followed by the addition of red blood cell lysate to eliminate the remaining red blood cells. Cells were then centrifuged at 1200 rpm for 5 min. The bone marrow-derived cells were collected after discarding the supernatant and resuspended in IMDM culture medium (Gibco) containing 10% % fetal bovine serum (FBS) (Gibco). The cells were then seeded uniformly into T75 culture flasks overnight to eliminate fast-adherent stromal cells. The following day, the supernatant was collected from the medium and centrifuged at 1200 rpm for 5 min to isolate anchorage-independent cells. These cells were then resuspended in IMDM medium containing 10% FBS and 20 ng/ml of recombinant mouse granulocyte macrophage colony-stimulating factor (GM-CSF) (novoprotein, CK02) to promote differentiation into macrophages. After 3–4 days of culture, the anchorage-dependent cells were identified as mouse bone marrow-derived macrophages (BMDMs).

2.3. Myelin debris preparation

Mouse myelin debris was prepared using a sucrose gradient centrifugation method, as described previously [35]. Specifically, 10–12 wild-type C57BL/6 mice, aged 8–10 weeks, were euthanized and their brains were immediately placed into sterile culture dishes. The meninges, cerebellum, and midbrain were removed, and the cerebral cortes were diced and homogenized in a 0.32 M sucrose solution. An additional 0.83 M sucrose solution was added to the brain homogenate, which was then centrifuged at 10,000 g for 45 min at 4 °C using an ultra-speed centrifuge. The white myelin debris located between the two sucrose gradient interfaces was collected, resuspended in Tris-Cl buffer, and centrifuged again at 10,000 g for 45 min at 4 °C. The supernatant was discarded, and the myelin debris was resuspended in sterile PBS and centrifuged again at 22,000 g for 10 min at 4 °C. The final myelin debris in the precipitate was collected. The myelin sheath fragments were then resuspended in sterile PBS to a final concentration of 100 mg/ml and stored at −80 °C for later use.

2.4. Myelin debris dil labelling

Before using myelin debris in the treatment of BMDMs, 100 mg/ml of myelin debris was first mixed with 10 μM Dil cell membrane red fluorescent probe (Beyotime, C1036) in PBS at room temperature for 10 min. The Dil-labelled myelin debris was then centrifuged at 10000 g for 10 min at 4 °C and washed once to remove the fluorescent probe. The

Dil-labelled myelin debris was then diluted back to 100 mg/ml for later use.

2.5. Mitochondria isolation

The Cell Mitochondria Isolation Kit (Beyotime, C3601) was used to isolate the mitochondria of BMDMs. Initially, BMDMs were cultured with trypsin and resuspended in PBS. Then, 1 ml of mitochondrial isolation reagent/10^7 cells was added and incubated for 15 min. The cell suspension was transferred to a glass homogenizer and homogenized 20 times. The homogenate was centrifuged at 1000 g, 4 °C for 10 min to obtain the supernatant, which was further centrifuged at 3500 g, 4 °C for 10 min. The supernatant was discarded and the pellet was collected as the isolated mitochondria. They were resuspended in 200 µl of mitochondrial storage solution and stored at −80 °C.

2.6. Transmission electron microscopy

The isolated mitochondria were centrifuged at 3500 g, 4 °C for 10 min. The supernatant was discarded and the pellet was double-fixed in 2.5% glutaraldehyde for 4 h. For spinal cord tissue TEM imaging, the animals were put under anesthesia and received transcardial perfusion with saline followed by 4% paraformaldehyde. The spinal cord at the site of injury was immediately collected and preserved in 2.5% glutaraldehyde for 4 h. Subsequently, the specimens were sliced into dimensions of $1 \times 1 \times 3$ mm^3 and double-fixed in a mixture of 2.5% glutaraldehyde.

Afterwards, specimens were shipped overnight at 4 °C to the Transmission electron microscopy (TEM) laboratory at the Pathology Department of Xiangya Hospital, Changsha, Hunan. The specimens were washed with Millonig's phosphate buffer solution (pH = 7.3), incubated in 1% osmium tetroxide for 1 h, and then washed again. After dehydration in acetone gradients (50%, 70%, and 90% for 10 min each, followed by two rounds of 100% acetone at 15-min intervals), the specimens were soaked in a 1:1 mixture of acetone and resin for 12 h. They were then embedded in 100% resin at 37 °C overnight. Once solidified, the specimens were polymerized at 37 °C overnight and then at 60 °C for 12 h. Ultrathin sections (90 nm) of the isolated mitochondria and spinal cord tissues were obtained using a UC-7 ultramicrotome (Leica) equipped with a diamond knife. Finally, the sections were double stained with 3% uranyl acetate and lead nitrate. They were both examined and photographed on a Hitachi HT-7700 electron microscope.

2.7. Construction of the engineered mitochondrial compound

The triphenylphosphonium cations – (cysteine-alanine-glutamine-lysine) (Tpp-CAQK) peptide was synthesized and quality checked by Sangon Biotech (Shanghai, China). Its chemical structure, as well as the results of HPLC and LCMS analysis, is listed in Supplementary Fig. 1. Tpp was attached to the C-terminus of the peptide, and a FAM fluorescent molecule was attached to the N-terminus. The Mito-Tpp-CAQK(FAM) compound was synthesized as described in previous works with modification [22]. Specifically, Tpp-CAQK (FAM) was dissolved in the mitochondrial storage solution, achieving a final concentration of 5 mg/ml 1 ml of Tpp-CAQK (FAM) solution was then mixed with 200 µl of mitochondrial solution derived from 10^7 cells and subjected to incubation on a rotating mixer at 4 °C for 45 min. After incubation, the mixture was incubated quiescently at 4 °C for 15 min to obtain the final engineered Mitochondrial (Mito)-Tpp-CAQK (FAM) compound solution for cell treatment and mouse intravenous injection. The compound was quantified to the final concentration of $2–5 \times 10^6$/ml with a Beckman counter.

2.8. Cell treatment

The extracted primary BMDMs were seeded in six-well plates at 10^5

cells/ml density. The cells were treated with 100 ng/ml of interleukin-10 (IL-10) (Novoprotein, C697) or IL-10 combined with 1 nM of Mertk inhibitor UNC2250 (Selleck, S7342) for 48 h before being collected for further analysis.

For Mito-Tpp-CAQK(FAM) compound treatment, 10 µl Mito-Tpp-CAQK(FAM) compound solution was added to 2 ml culture medium.

In the myelin debris uptake experiment, cells were treated with a 1 mg/mL solution of myelin debris as previously described [21] and were incubated for 48 h.

2.9. Animals

Female C57BL/6 mice (8 weeks old, weight 20–25 g) were used in this study. The animals were purchased from Hunan SJA Laboratory Animal Company Limited and were kept in a pathogen-free animal facility at Central South University, following standard purification procedures. They were housed in the laboratory animal unit, with a 12-h day/night cycle, and were provided ad libitum access to food and water. The mice were allowed to acclimatize to the new environment for one week before undergoing the surgical procedure.

2.10. Spinal cord contusive injury model and treatment

The Animal Care and Use Committee of Central South University, Changsha, China, approved all animal protocols and experimental procedures. To anesthetize mice, intraperitoneal injection of 0.5 ml 0.3% sodium pentobarbital was administered. Prior to surgery, the skin was prepared, and disinfected, and the area was draped. The skin was then incised at the center of the T10 spinous process, and the muscles adjacent to the spinous process were separated. Next, the T10 spinous process and lamina were dissected to expose the spinal cord. The modified Allen's percussion method (50 kdyne) was used to establish the spinal cord contusion model [36]. The spinal cord injury model was successfully established when local hematoma was observed in the spinal cord tissue, and the lower limbs and tail of the mice were twitching. Following this, the muscle, fascia, and skin were sutured layer by layer using 4-0 suture, and the skin was sterilized with iodine. A sham group was also created, where mice were only exposed to spinal cord tissue without any contusive injury. After the surgical procedure, mice were placed on a heating pad to maintain body temperature until they woke up. They were then housed in cages with 4–5 mice per cage, with adequate food and drinking water provided. Penicillin was administered via intramuscular injection twice a day for three days after the operation to prevent infection. The mice's bladders were manually pressed for seven consecutive days post-surgery.

For the Mito-Tpp-CAQK compound treatment of mice, three groups were established: the sham group, the control group (which was administered two intravenous injections of 200 µl of saline on the third and fifth days after injury), and the experimental group (which was administered two intravenous injections of 200 µl of Mito-Tpp-CAQK compound solution on the third and fifth days after injury).

2.11. Flow cytometry and ROS detection

The BMDMs cultured on a six-well plate were harvested. After treatment, they were fixed with fixation buffer (Biosciences, 554,655) for 20 min at 4 °C, permeabilized with 0.1% Triton for 10 min, and blocked with 3% bovine serum albumin (BSA) for 20 min. Then, the cells were incubated with CD11b-FITC (Proteintech, FITC-65055), F4/80-APC (eBioscience, MF48005), Mertk-PE (eBioscience, 12-5751-82) for 30 min followed by analysis using a BD FACSAria III flow cytometer (BD Biosciences). For intracellular Reactive Reactive Oxygen Species (ROS) detection, cells were stained with 2′,7′-dichloro-fluorsecein-diacetate (DCFH-DA) from the Reactive Oxygen Species (ROS) assay kit (Beyotime Biotechnology, S0033S) and then analyzed by flow cytometry according to the manufacturer's protocol. The data were quantitatively analyzed

using FlowJo V10.

2.12. ATP and pyruvate kinase assay

The cells were harvested and homogenized with a glass homogenizer. The protein concentration was determined by employing the BCA Protein Assay Kit (Elabscience, E-BC-K318-M). ATP levels (Beyotime, S0026) and Pyruvate kinase (PK) specific activity (Elabscience, E-BC-K611-M) were measured and calculated according to the instructions provided by the manufacturer.

2.13. Western blotting

Cellular proteins were extracted using RIPA buffer infused with protease and phosphatase inhibitors. The protein concentrations were quantified using the BCA Protein Assay Kit. Subsequently, the proteins were separated by SDS-PAGE gels and transferred onto a polyvinylidene fluoride membrane (Millipore, Billerica, MA). The membrane was blocked with 5% milk in TBST for 90 min at room temperature before being incubated with primary antibodies overnight at 4 °C. The primary antibodies and their respective dilutions employed were as follows: (Tomm40, Proteintech, 18409-1-AP, 1:2000; COX III, Proteintech, 55082-1-AP, 1:800; COX IV, Proteintech, 11242-1-AP, 1:4000; p21, Abcam, ab188224, 1:1000; p53, Abcam, ab26, 1:1000; iNOS, Proteintech, 18985-1-AP, 1:2000; Arg1, Proteintech, 16001-1-AP, 1:1000; IL-6, Santa Cruz, sc-57315,1:500; IL-1β, Santa Cruz, sc-12742, 1:500; β-actin, Proteintech, 66009-1-Ig, 1:10,000). After being rinsed five times with TBST, the membrane was incubated with peroxidase-conjugated goat anti-rabbit or anti-mouse IgG secondary antibodies (Elabscience, E-AB-1003/E-AB-1001, 1:10,000). Finally, using the chemiluminescence reagent (ShareBio, SB-WB001), the immunoreactive bands were visualized with a ChemiDoc XRS Plus luminescent image analyzer (Bio-Rad, England). The image analysis was performed using ImageJ software, and the relative expression levels of the target proteins to β-actin were used for statistical comparison.

2.14. JC1 staining

The isolated mitochondria or mitochondrial compounds were stained with JC-1 staining solution (Mitochondrial Membrane 347 Potential Assay Kit containing JC-1, Elabscience, E-CK-A301) according to the manufacturer's protocol and then spotted onto slides. The fluorescent images were acquired using a confocal microscope (Zeiss). The JC1 ratio (red/green) was quantitatively analyzed using Image J.

2.15. Mitotracker red labelling

When detecting cellular mitochondria, cells were incubated with Mitotracker Red CMXRos (Beyotime, C1035) at 37 °C for 30 min according to the manufacturer's protocol. For treating BMDMs with Mito-Tpp-CAQK compounds or labelling mitochondria injected into mice *in vivo*, the compounds were pre-incubated with Mitotracker Red for 30 min. The fluorescent images were acquired using a confocal microscope (Zeiss) and analyzed with Image J to quantify mitochondrial fluorescence intensity.

2.16. Cell mito stress test

The Seahorse FX96 Extracellular Flux Analyzer (Seahorse Biosciences, North Billerica, MA, USA) was employed according to the manufacturer's protocol. BMDMs were seeded in XF96 cell culture plates at a density of 5000 cells per well 48 h before the experiment and treated with different myelin debris and mitochondrial compounds. During the measurement, the Oxygen Consumption Rates (OCR) of BMDMs were tested by sequentially adding 1.5 μM oligomycin (an ATP synthase blocker), 1 μM carbonyl cyanide 4-(trifluoromethoxy) phenylhydrazone (FCCP, the mitochondrial uncoupler), 0.5 μM antimycin A and 0.5μM rotenone (A&R, inhibitors of mitochondrial complex I and III). The XFe-Wave software (Seahorse Biosciences) was used to quantify the results. The basal respiration, ATP production, and Spare respiratory capacity (maximal electron transport chain activity) were calculated as described previously using the XFe Cell Mito Stress Test Report Generator.

2.17. Immunofluorescence assay, oil red O staining, and H&E staining

For immunofluorescence assay, frozen sections of 16-μm thickness from the spinal cord containing the lesion site were harvested at 7, 14, and 28 days post-SCI (or sham group) and cut along the sagittal plane. The frozen sections were rewarmed at room temperature for 15 min and rinsed three times with a PBS solution for 10 min each time. The immunohistochemical pen was used to circle the spinal cord sections on the slides. The sections were then permeabilized with 100 μL of PBS solution containing 0.1% Tween 20 and 0.3% Triton-X 100 for 30 min and blocked with 5% BSA in PBS for an additional 30 min. After blocking, the sections were incubated with a group of primary antibodies including 4-Hydroxynonenal (4-HNE) (Abcam, ab48506, 1:200), F4/80 (Abcam, ab6640, 1:400), MBP (CST, 78,896, 1:400), TUJ-1 (CST, 5568, 1:400), GFAP (Proteintech, 16825-1-AP, 1:800), iNOS (Proteintech, 18985-1-AP, 1:200), Arg1 (Proteintech, 16001-1-AP, 1:200), Neun (Abcam, ab177487, 1:400), and Oligo2 (Proteintech, 13999-1-AP, 1:400) overnight at 4 °C. After being rinsed five times for 10 min each with PBS containing 0.1% Tween 20, the sections were incubated for 1 h at room temperature with species-appropriate secondary antibodies conjugated with Alexa Fluor 594 (Abcam, 1:400) or Alexa Fluor 488 (Abcam, 1:400). Subsequently, the sections were rinsed with PBS containing 0.1% Tween 20 before being mounted on slides and covered with DAPI (Genetex). The sections were analyzed under a fluorescence microscope or confocal microscope (Zeiss). To validate antibody specificity and distinguish genuine target staining from the background, secondary antibody-only controls were employed. The ImageJ software was used for quantitative analysis of the images, while the Imaris 9.0 software was used for 3D reconstruction.

The Modified Oil Red O Staining Kit (Beyotime, C0158S) according to the manufacturer's instructions. For Hematoxylin & Eosin (HE) staining, mice were euthanized and the heart, liver, spleen, lungs, kidneys, and bladder tissues were excised. The bladder at 28 days post-injury was emptied of urine prior to macroscopic photography. These organs were fixed in formalin, dehydrated using an ethanol gradient, embedded in paraffin, sectioned, and subsequently stained with the Hematoxylin and Eosin Staining Kit (Beyotime, C0105S) according to the manufacturer's instructions. The tissue sections after staining were captured using an inverted microscope (Nikon) and analyzed using ImageJ software.

2.18. In vivo imaging

After 72 h of injury, the mice received different injections intravenously. The injections included 1) 200 μl of saline, 2) 200 μl of saline with 1 μl of dioctadecyl-3,3,3,3-tetramethylindotricarbocyanine iodide (DiR) (100 μg/ml, Invitrogen), 3) 200 μl of isolated mitochondrial solution with 1 μl of DiR, or 4) 200 μl of Mito-Tpp-CAQK (without FAM modification) compound solution with 1 μl of DiR. Imaging was done at 12, 24, and 48 h after injection using the IVIS Spectrum (Perklin Elmer, Germany) instrument with excitation at 754 nm and emission at 778 nm. At 48 h after injection, the mice were euthanized and their brain, spinal cord, lung, kidney, liver, spleen, stomach, bladder, ileum, and serum were collected and imaged using the IVIS Spectrum instrument with excitation at 754 nm and emission at 778 nm. Fluorescence intensity was processed statistically and quantified using the IVIS Living Image software.

2.19. Electrophysiology

Electromyography was conducted on 28 dpi to assess the motor-evoked potentials (MEPs) of the mice. The mice were anesthetized by intraperitoneally injecting them with 0.5 ml 0.3% sodium pentobarbital. To assess the motor-evoked potentials (MEPs) of mice, a positive stimulating electrode was positioned on the motor area of the cerebral cortex's skull surface, accompanied by a negative stimulating electrode near the orbital bones. Further, a recording electrode was inserted into either the left or right gastrocnemius muscle, a reference electrode was inserted into the distal tendon of the hind limb muscle, and a ground electrode was placed under the back skin. The mice were then stimulated with a 3-mA single square wave (2 Hz) for 0.2 ms, and the amplitude of the hind limbs was recorded by calculating from the initiation point of the first response wave to the highest peak.

2.20. BMS score evaluation, LSS swimming, and grid walking test

To evaluate the functional recovery of hindlimb motor function in SCI mice, the Basso Mouse Scale (BMS) score evaluation system was used as previously described [37]. This assessment was carried out preinjury and on days 1, 3, 7, 14, and 28 dpi. The BMS scores ranged from 0 to 9, with 0 indicating complete paralysis and 9 indicating normal movement function of the hindlimbs. Prior to scoring, the mice were placed on the test table to acclimate to the environment. Each mouse was observed for 4 min.

The mice underwent a training period of three consecutive days to swim in a water-filled tank sized 5×15 cm, moving from one side to the other. After this training period, surgery was performed. On the 28th day post-surgery, the mice were placed in the same tank and observed for a duration of 30 s. The Louisville Swim Scale (LSS) swim score was used to assess the mice's swimming ability, which involved evaluating hindlimb movement, hindlimb alternation, forelimb dependency, trunk stability, and body angle [38].

The mice were trained to walk on a grid box (20×30 cm in size with 2×2 cm squares, 30° slope) for three consecutive days before surgery. On 28 dpi, the mice were placed at the bottom of the grid box. The number of hindlimb falling (errors) from the grid for the duration of 100 steps from the bottom to the top was counted.

Two trained observers, who were blinded to the grouping of the mice, simultaneously observed and recorded the BMS score, LSS score, and Grid walking error numbers. The average of the scores from the two observers was recorded as the final score.

2.21. Statistical analysis

The statistical analysis of the results was performed using GraphPad Prism (version 7.0, USA). All data were reported as mean ± standard deviation (SD). Normality was determined using the Shapiro-Wilk test. For group number = 2, the homogeneity of variances was tested using the F-test. When the data followed a normal distribution and homogeneity of variance, an unpaired t-test was conducted for the statistical analysis. For group number >2, the homogeneity of variances was tested using the Brown-Forsythe test. When the data followed a normal distribution and homogeneity of variance, an ordinary one-way ANOVA and Tukey's multiple comparisons test were performed for the statistical analysis. Two-way ANOVA was utilized for data with two variables, grouping and time.

All differences among and between groups were considered statistically significant at $p < 0.05$. In the figures, ns denotes $p \geq 0.05$, * denotes $p < 0.05$, ** denotes $p < 0.01$, *** denotes $p < 0.001$, and **** denotes $p < 0.0001$.

3. Results

3.1. IL-10-induced mertk^{hi} macrophages show enhanced mitochondrial function

Mertk is a key molecule that mediates the phagocytic activity of macrophages and is closely related to glycolytic metabolism [39,40]. Analysis of the single-cell dataset GSE162610 after spinal cord injury in mice revealed that Mertk is mainly expressed in myeloid cells, especially macrophages, and its expression decreases after spinal cord injury (Fig. 1A), which indicates the dysfunction of macrophages following SCI. We extracted primary bone marrow-derived macrophages (BMDMs) from mice and induced them into M2c-type macrophages using interleukin-10 (IL-10). Flow cytometry showed that the purity of BMDMs in the extracted cells was 95.1%, with a proportion of Mertk-positive macrophages of 75.7%. Under IL-10 induction, the proportion of Mertk-positive macrophages increased to 93.5%, indicating a significant increase in Mertk expression (Fig. 1B and C). The macrophages with high expression of Mertk (Mertk^{hi}), induced by IL-10, exhibited significantly increased levels of ATP and pyruvate kinase. However, the concurrent use of a Mertk inhibitor (UNC2250) reversed this increase (Fig. 1D and E). The detection of the mitochondrial membrane proteins Tomm40 and cytochrome *c* oxidase subunit III/IV (COX III/COX IV) showed an increase in their expression levels following IL-10 induction (Fig. 1F and G). Furthermore, there was a significant increase in the content of mitochondrial DNA (mtDNA) in IL-10-induced macrophages (Fig. 1H). Mertk inhibitor reversed the increase in these mitochondrial-related proteins and mtDNA (Fig. 1F–H).

This indicates that IL-10 induced Mertk^{hi} macrophages have an enhanced mitochondrial function, and this enhancement is associated with the upregulation of Mertk expression. In addition, both MBP immunostaining and Dil-labelled myelin debris phagocytosis experiments confirmed that Mertk^{hi} macrophages also have an increased phagocytic capability (Supplementary Fig. 2), consistent with their elevated mitochondrial function. Therefore, we utilized IL-10-induced Mertk^{hi} macrophages as donor cells for mitochondrial transplantation.

3.2. Construction of the mitochondria-Tpp-CAQK compound for transplantation

To improve the targeting specificity of mitochondrial delivery, the targeting peptide named cysteine-alanine-glutamine-lysine (CAQK) was used. Triphenylphosphonium cations (Tpp$^+$) were synthesized at the C-terminus of CAQK, enabling them to insert into the outer membrane of mitochondria. The chemical structure of Tpp-CAQK, as well as the HPLC and LCMS results, are provided in Supplementary Fig. 1. Initially, BMDMs were extracted and induced into Mertk^{hi} macrophages using IL-10. Following this, the mitochondria were isolated from these cells. The CAQK targeting peptide, conjugated to TPP, was then co-incubated with the mitochondria, resulting in the formation of the Mito-Tpp-CAQK compound (Fig. 2A). TEM images showed that the isolated mitochondria (red arrows) displayed well-defined mitochondrial cristae structures (Fig. 2B). Furthermore, co-localization of the mitotracker red-labelled mitochondria with the FAM fluorescent-labelled Tpp-CAQK structure was observed in the Mito-Tpp-CAQK compound. The Tpp-CAQK peptide was observed to overlap with the mitochondrial structure, as indicated by the white arrows (Fig. 2C). To test the bioenergetic potential of the mitochondrial compound, JC1 staining was applied. In fresh isolated mitochondria, JC1 mainly existed in the form of JC1 aggregates (red), while after the use of the uncoupler Carbonyl cyanide 3-chlorophenylhydrazone (CCCP) induced mitochondrial depolarization, large amounts of JC1 monomer (green) were formed (Fig. 2D). The results indicated that the constructed Mito-Tpp-CAQK compound has no significant decrease in mitochondrial membrane potential (Fig. 2E), showing good bioenergetic potential. Following treatment of macrophages with the mitotracker red pre-labelled Mito-Tpp-CAQK compound
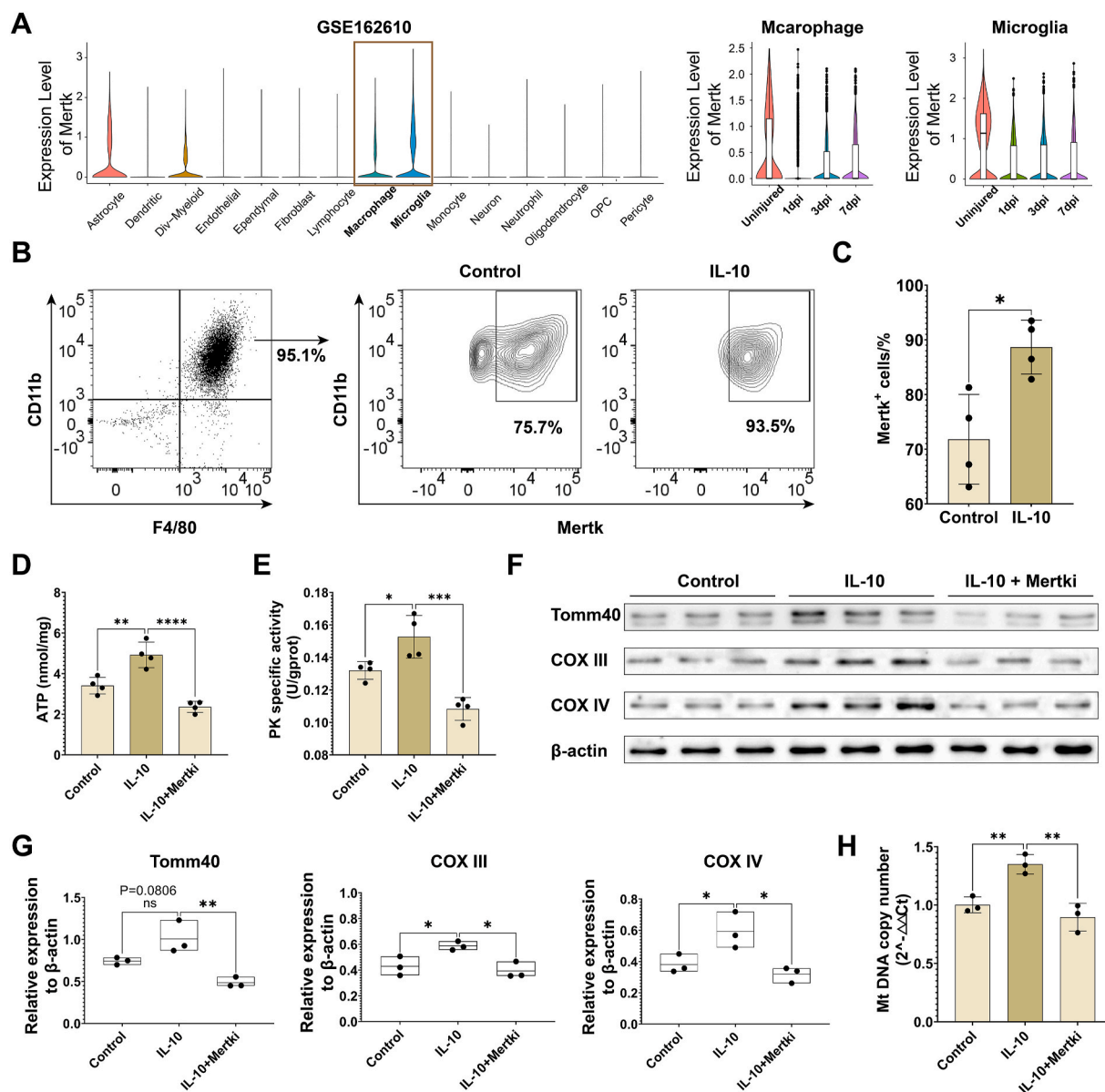
Fig. 1. IL-10-induced Mertk^{hi} macrophages show enhanced mitochondrial function. (A) The expression level of Mertk in different cell types, as well as in macrophage and microglia in different time point post injury, in single-cell dataset GSE162610. **(B)** Flow cytometry analysis of CD11b, F4/80, and Mertk on bone marrow-derived macrophages. **(C)** Quantification of the Mertk$^+$ cell proportion in (B) (n = 4, mean ± SD, unpaired t-test, *p < 0.05). **(D)** Adenosine Triphosphate (ATP) contents in treated cells (n = 4, mean ± SD, one-way ANOVA, Tukey's multiple comparisons, **p < 0.01 ****p < 0.0001). **(E)** Pyruvate kinase (PK) specific activity in treated cells (n = 4, mean ± SD, one-way ANOVA, Tukey's multiple comparisons, *p < 0.05 ***p < 0.001). **(F)** Western blotting analysis of the levels of Tomm40, COX III, COX IV, and β-actin in BMDMs with different treatments. **(G)** Quantification of the relative expression of Tomm40, COX III, and COX IV to β-actin in (F) (n = 3, mean ± SD, one-way ANOVA, Tukey's multiple comparisons, *p < 0.05). **(H)** MtDNA copy number calculated with the 2^-△△Ct method in treated cells (n = 3, mean ± SD, one-way ANOVA, Tukey's multiple comparisons, **p < 0.01).

for 6 h, it was observed that the mitochondrial compound was taken up into macrophages (Fig. 2F). These results show that we have successfully constructed a mitochondrial compound suitable for mitochondrial transplantation.

3.3. Mertk^{hi} mac-Mito-Tpp-CAQK improves macrophage phagocytosis of myelin debris

To investigate the impact of Mito-Tpp-CAQK on macrophage phagocytic function in vitro, we treated BMDMs with pre-prepared myelin debris at a concentration of 1 mg/ml. We then added mac-Mito-Tpp-CAQK, Mertk^{hi} **mac**-Mito-Tpp-CAQK, or Mertk^{hi} **mac**-Mito-Tpp-CAQK with CCCP and observed the resulting effects. After 48 h of

treatment, double immunofluorescence staining of MBP and F4/80 was performed. The results showed that in the control group, macrophages marked by F4/80 only phagocytized a small amount of myelin debris, while a large amount of myelin debris remained on the cell membrane surface (Fig. 3A). However, in the experimental group treated with Mito-Tpp-CAQK, myelin debris was engulfed into the cytoplasm of macrophages, and the mitochondrial compounds derived from Mertk^{hi} macrophages significantly increased the uptake of myelin debris (Fig. 3A, C). Nonetheless, when CCCP was added to impair mitochondrial function, macrophage uptake of myelin debris significantly decreased (Fig. 3A, C).

In addition, to observe the process of lipid engulfment, we conducted a phagocytosis experiment using Dil-labelled myelin debris. Similar results were observed, where treatment with Mito-Tpp-CAQK significantly
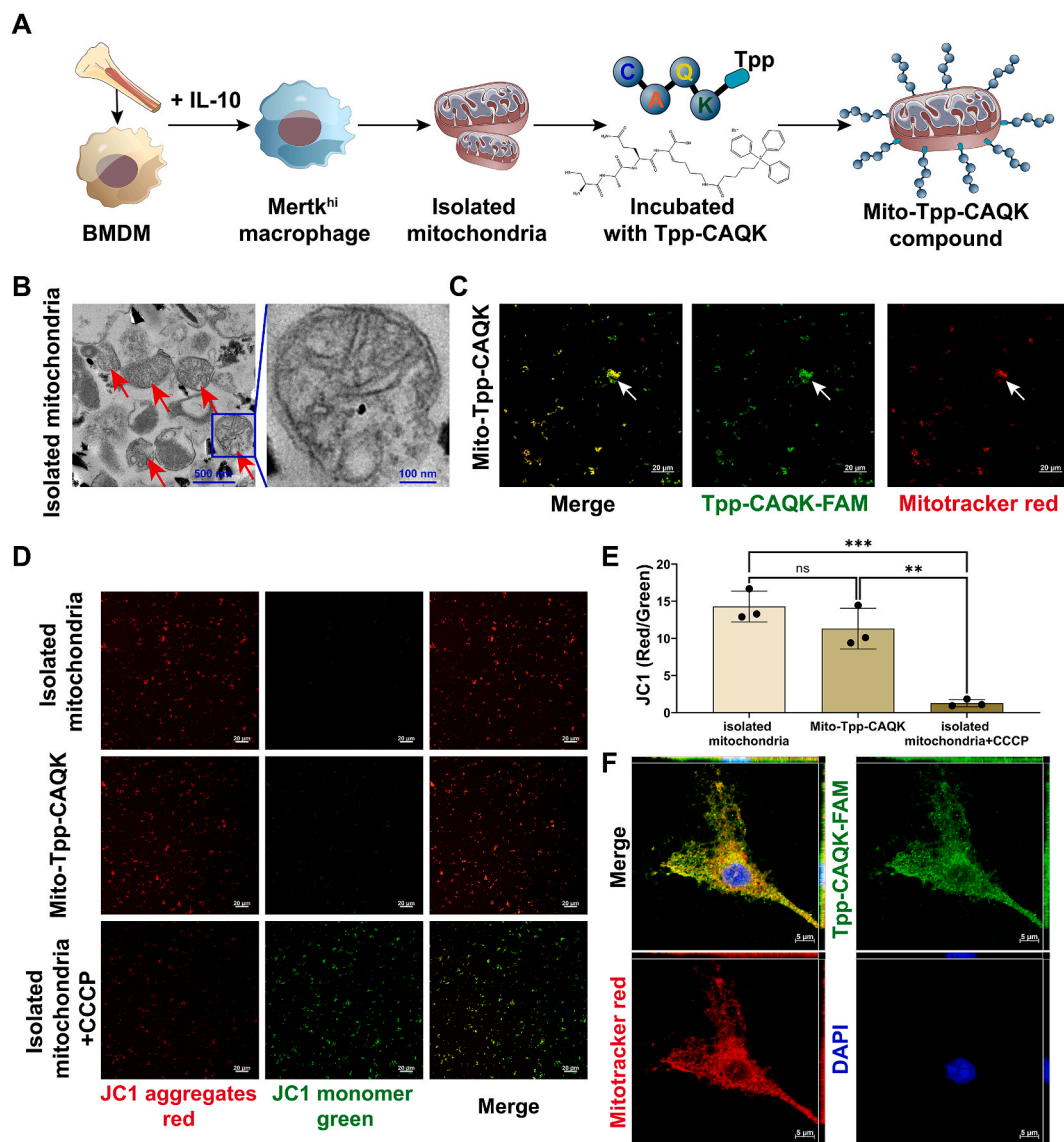
Fig. 2. Construction of the mitochondria-Tpp-CAQK compound for transplantation. (A) Experimental flowchart showing the construction process of the mitochondria-triphenylphosphonium cations-cysteine-alanine-glutamine-lysine (Mito-Tpp-CAQK) compound. **(B)** Transmission Electron Microscope (TEM) showing the structure of isolated mitochondria from BMDMs (scale bar = 500/100 nm, red arrows: isolated mitochondria). **(C)** Confocal images of mitotracker red labelled Mito-Tpp-CAQK-FAM (red: mitotracker red, green: Tpp-CAQK-FAM, scale bar = 20 μm). **(D)** Representative confocal images of JC1 stained isolated mitochondria, Mito-Tpp-CAQK, and isolated mitochondria + Carbonyl cyanide 3-chlorophenylhydrazone (CCCP) (red: JC1 aggregates, green: JC1 monomer, scale bar = 20 μm). **(E)** Quantification of the JC1 aggregates/monomer ratio in (D) (n = 3, mean ± SD, one-way ANOVA, Tukey's multiple comparisons, ns not significant **p < 0.01 ***p < 0.001). **(F)** Confocal images showing BMDMs internalizing the Mito-Tpp-CAQK compound after 6 h of treatment (red: mitotracker red, green: Tpp-CAQK-FAM, blue: DAPI, scale bar = 5 μm).

increased macrophage uptake of lipids in the myelin debris. This phagocytic capability of BMDMs was most pronounced in the Mertk[hi] mac-Mito-Tpp-CAQK experimental group (Fig. 3B, D). Furthermore, the 3D view showed that in the Mertk[hi] mac-Mito-Tpp-CAQK group, a large number of myelin debris was engulfed and digested into small lipid droplets, unlike the large lipid droplets observed in the other groups. These findings suggest that Mito-Tpp-CAQK, particularly Mertk[hi] **mac**-Mito-Tpp-CAQK, can enhance macrophage phagocytosis of myelin debris (Fig. 3C and D). Therefore, in subsequent experiments, we used Mito-Tpp-CAQK derived from Mertk[hi] BMDMs.

3.4. Mito-Tpp-CAQK alleviates the mitochondrial dysfunction and pro-inflammatory profile of macrophages following phagocytosis

The mitochondrial dysfunction of immune cells leads to their

functional impairments and phenotypic changes. Moreover, after spinal cord injury, M1-type macrophages, which are pro-inflammatory, contribute significantly to the inhibitory microenvironment. Therefore, we investigated whether phagocytosis of myelin debris by macrophages leads to cellular mitochondrial dysfunction and increased pro-inflammatory responses. After labeling the cell mitochondria with mitotracker red, we discovered that the density and area of the mitochondria decreased in macrophages after 48 h of exposure to myelin debris. However, treatment with Mito-Tpp-CAQK resulted in a significant increase in both the density of mitochondria (Fig. 4A and B). For mitochondrial respiration, OCR measurements showed a significant decrease in basal respiration, maximal respiration, ATP production, and spare respiratory capacity in macrophages after myelin debris processing (blue and red group). Supplementation with mitochondrial compounds after myelin debris treatment significantly restored basal
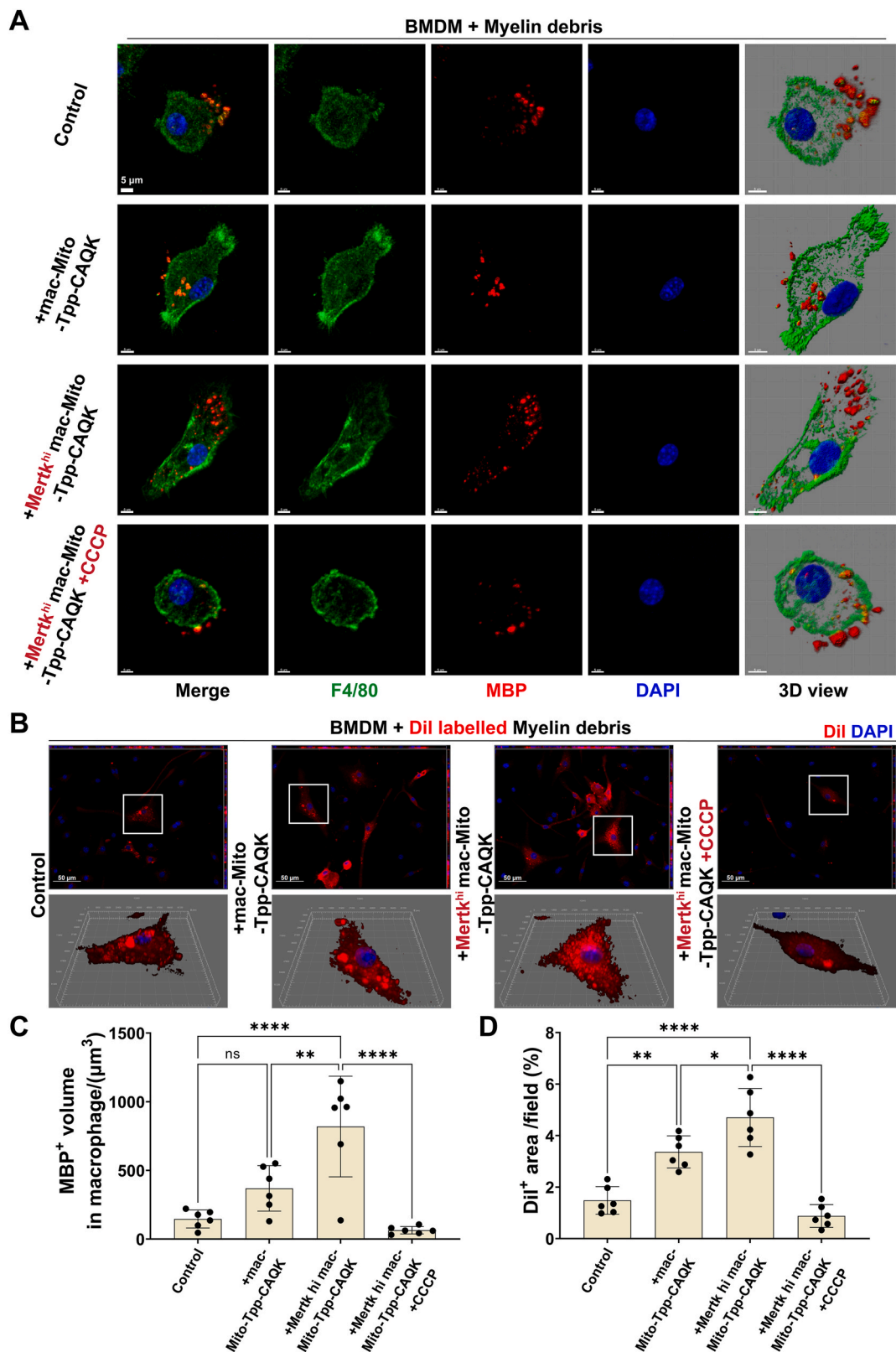
Fig. 3. Mertk[hi] mac-Mito-Tpp-CAQK improves macrophage phagocytosis of myelin debris. (A) Representative confocal images showing double immunofluorescence staining and 3D view of F4/80 and (Myelin Basic Protein) MBP on myelin debris treated BMDMs in four groups (green: F4/80, red: MBP, blue: DAPI, scale bar = 5 μm). **(B)** Representative confocal images and enlarged 3D view of Dil-labelled myelin debris within BMDMs in four groups (red: Dil, blue: DAPI, scale bar = 50 μm, the length of each grid in the 3D view: 5 μm). **(C)** Quantification of the MBP[+] volume in F4/80-labelled macrophages from (A) (n = 6, average of each field, mean ± SD, one-way ANOVA, Tukey's multiple comparisons, ns not significant **p < 0.01 ****p < 0.0001). **(D)** Quantification of the Dil[+] area in macrophages per field from (B) (n = 6, fields in maximal intensity projection images, mean ± SD, one-way ANOVA, Tukey's multiple comparisons, *p < 0.05 **p < 0.01 ****p < 0.0001).
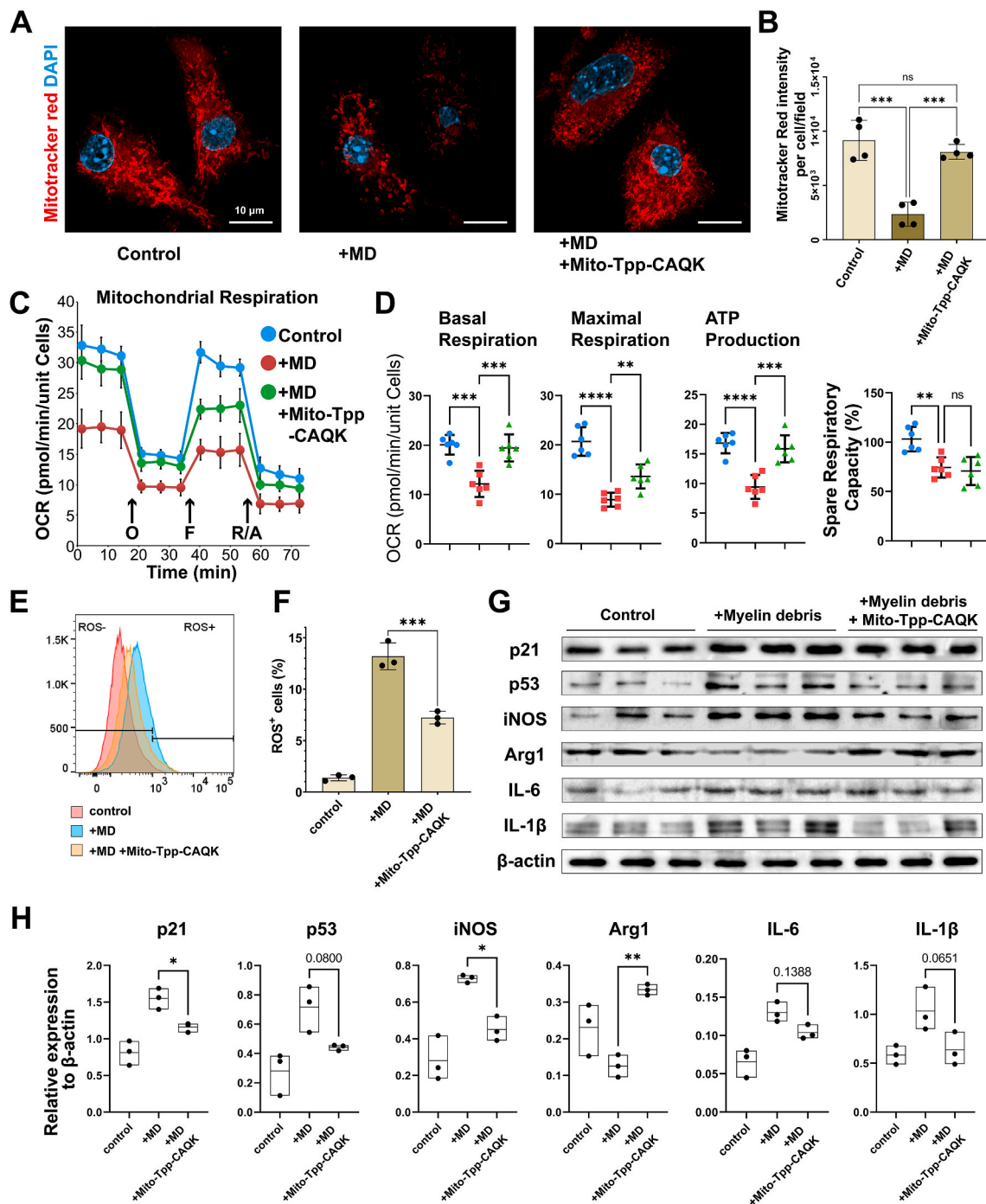
Fig. 4. Mito-Tpp-CAQK alleviates the mitochondrial dysfunction and pro-inflammatory profile of macrophages following phagocytosis. (A) Representative confocal images showing the mitotracker red labelled BMDMs under treatment (red: mitotracker red, blue: DAPI, scale bar = 10 μm, MD: myelin debris) **(B)** Quantification of the mitotracker red intensity per cell each field from (A) (n = 4, mean ± SD, one-way ANOVA, Tukey's multiple comparisons, ns not significant ***p < 0.001). **(C)** OCR measurement results for mitochondrial respiration assessment in BMDMs (n = 6, mean ± SD, OCR: oxygen consumption rate, O: oligomycin, F: FCCP, R/A: rotenone & antimycin A). **(D)** Quantification of the OCR measurement from (C) (n = 6, mean ± SD, one-way ANOVA, Tukey's multiple comparisons, ns not significant **p < 0.01 ***p < 0.001 ****p < 0.0001). **(E)** Flow cytometry indicating the intracellular ROS level of cells by DCFH-DA staining. **(F)** Quantification of intracellular ROS level in (E) (n = 3, mean ± SD, one-way ANOVA, Tukey's multiple comparisons, ***p < 0.001). **(G)** Western blotting analysis of the levels of p21, p53, iNOS, Arg1, IL-6, IL-1β, and β-actin in BMDMs with different treatments. **(H)** Quantification of the relative expression of p21, p53, iNOS, Arg1, IL-6, and IL-1β to β-actin in (G) (n = 3, mean ± SD, one-way ANOVA, Tukey's multiple comparisons, *p < 0.05 **p < 0.01).

respiration, maximal respiration, and ATP production. Nonetheless, there was no change observed in the spare respiratory capacity of the macrophages (green group) (Fig. 4C and D).

Flow cytometry detected comparable results regarding intracellular ROS levels, showing that treatment with the mitochondrial compound reduces the accumulation of ROS induced by myelin debris (Fig. 4E and

F). Meanwhile, treatment with myelin debris led to a significant increase in the expression of p21 and p53, indicating cellular injury and stress state. This was accompanied by an increase in the expression of the pro-inflammatory protein iNOS and a decrease in the expression of the anti-inflammatory protein ARG1. These macrophages also showed increased expression of pro-inflammatory cytokines, such as IL-6 and IL-1β,

indicating a shift towards M1 phenotype (Fig. 4G and H). However, upon the addition of Mito-Tpp-CAQK, a significant reduction in the expression of p21 and p53 was observed. Additionally, the expression of iNOS, IL-6 and IL-1β was decreased. These changes were accompanied by an increase in the expression of the anti-inflammatory marker ARG1, suggesting that the Mito-Tpp-CAQK compound can and promote macrophage transition towards an M2 phenotype (Fig. 4G and H). This indicates that the Mito-Tpp-CAQK compound noticeably mitigates the mitochondrial dysfunction and inflammatory responses resulting from macrophages' phagocytosis of substantial amounts of myelin debris.

3.5. Intravenous transplantation of Mito-Tpp-CAQK targeted the epicenter of injured spinal cord

To validate the specificity of Mito-Tpp-CAQK in targeting the injured spinal cord, we administered tail vein injections of saline, cell membrane dye Dir, Dir-labelled mitochondria, as well as Dir-labelled Mito-Tpp-CAQK compound starting from 3 dpi. We continuously monitored the fluorescence intensity changes in mice and various organs with *in vivo*

imaging (Fig. 5A and B). Results showed that mice injected with saline did not display any detectable fluorescence signal, and no labeling was found in the dissected tissues. Mice injected solely with Dir only had weak signals at the injury site, which increased 24 h post injection, but weakened after 48 h, and no significant fluorescence signal was found in the dissected spinal cord. In the Dir-Mito group, fluorescence signals were observed at the injury site 24 and 48 h post injection, and in the dissected spinal cord. Noticeably, in the Dir-Mito-Tpp-CAQK group, strong fluorescence signals were detected at the injury site as early as 12 h post-injection, and persisted for up to 48 h, with significant signals still present in the dissected spinal cord. Radiant efficiency of the Dir-Mito-Tpp-CAQK group was significantly higher than the Dir-Mito group (Fig. 5A and B). After 48 h of injection, the major organs of mice were dissected and arranged as depicted in Fig. 5C. In the Dir-Mito-Tpp-CAQK group, the dissected spinal cord exhibited the highest radiant efficiency, significantly higher than the Dir-Mito group (Fig. 5D). Through quantitative analysis of radiant efficiency in major organs *in vivo*, in the Dir-Mito-Tpp-CAQK group, an increase in the radiant efficiency of the spinal cord compared to other organs was shown (Fig. 5E). These results
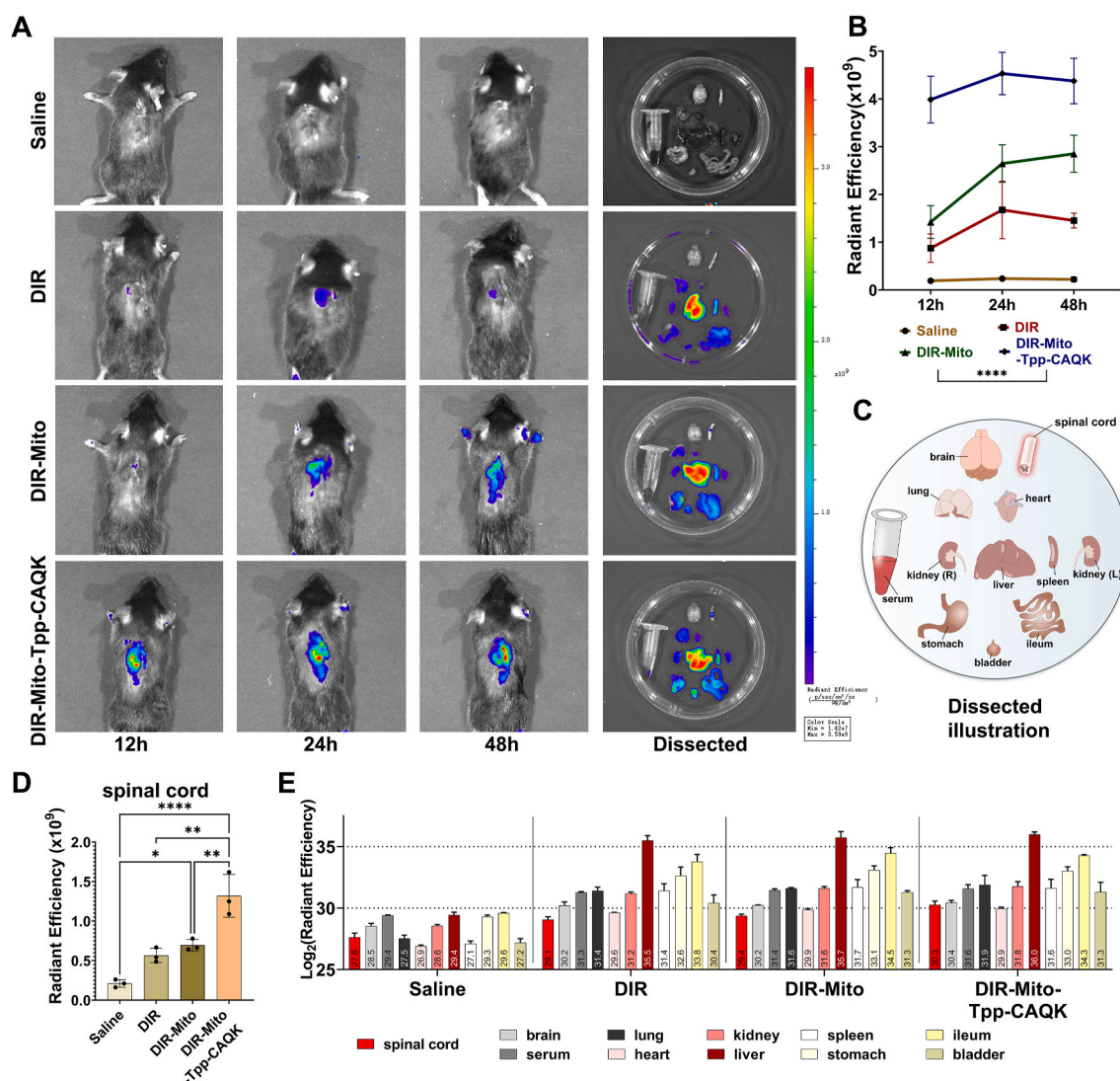

Fig. 5. Intravenous transplantation of Mito-Tpp-CAQK targeted the epicenter of injured spinal cord. (A) Representative *in vivo* images of C57BL/6 mice captured at 12 h, 24 h, and 48 h, as well as images of dissected organs, after intravenous injection of saline, DIR, DIR-Mito, and DIR-Mito-Tpp-CAQK (color gradient: radiant efficiency). **(B)** Quantification of the radiant efficiency in the target region of mouse in the saline, DIR, DIR-Mito, and DIR-Mito-Tpp-CAQK groups at 12 h, 24 h, and 48 h after injection (n = 3, mean ± SD, two-way ANOVA, ****p < 0.0001). **(C)** Illustration of the placement of the main organs of dissected mice. **(D)** Quantification of the radiant efficiency of the dissected spinal cord in (A) (n = 3, mean ± SD, one-way ANOVA, Tukey's multiple comparisons, *p < 0.05 **p < 0.01 ****p < 0.0001). **(E)** Quantification of the $\log_2$ (radiant efficiency) of the dissected organs in (A) (n = 3, mean ± SD).

confirm the efficacy of the engineered Mito-Tpp-CAQK compound in specifically delivering mitochondria to the site of spinal cord injury.

Considering the high radiant efficiency in the liver and other organs, we conducted HE staining on the hearts, livers, spleens, lungs, and kidneys of mice after administering the experimental dose (200μl; 5×10^6/ml) or double experimental dose of the compounds. The histopathology images showed no damage to cardiomyocytes, hepatic cells, splenic tissues, alveolar cells, or renal glomeruli, confirming the biocompatibility and safety of the engineered mitochondrial compounds (Supplementary Fig. 3).

3.6. The transplanted mitochondria compounds are mainly uptake by macrophages

To explore the identity of the cells that uptake dynamic mitochondria in the injured epicenter, we in vitro labelled the Mito-Tpp-CAQK compound with mitotracker red and subsequently conducted in vivo administration at 3 dpi, with detection on 7 dpi (Fig. 6A). In the sham group, mitochondria were almost absent from spinal cord tissue. In contrast, in the surgical group, fluorescence intensity of mitotracker red significantly increased on 7 dpi (Fig. 6B and C). Dual immunofluorescence with cell markers TUJ-1, GFAP and F4/80 showed that only a minimal number of mitochondria labelled by mitotracker red permeated TUJ-positive neuronal axons, and there were no indications of mitotracker-positive regions within GFAP-positive astrocytes. Large amounts of mitochondria were present in F4/80-labelled macrophages (Fig. 6D). By magnifying the image, it was evident that there was co-localization of mitotracker-positive mitochondria and F4/80-labelled macrophages (Fig. 6E). The fluorescence intensity of mitotracker red-positive regions in F4/80-labelled macrophages was the strongest, significantly higher compared to that of TUJ-1-labelled neurons and GFAP-labelled astrocytes (Fig. 6F). Therefore, we demonstrated that the
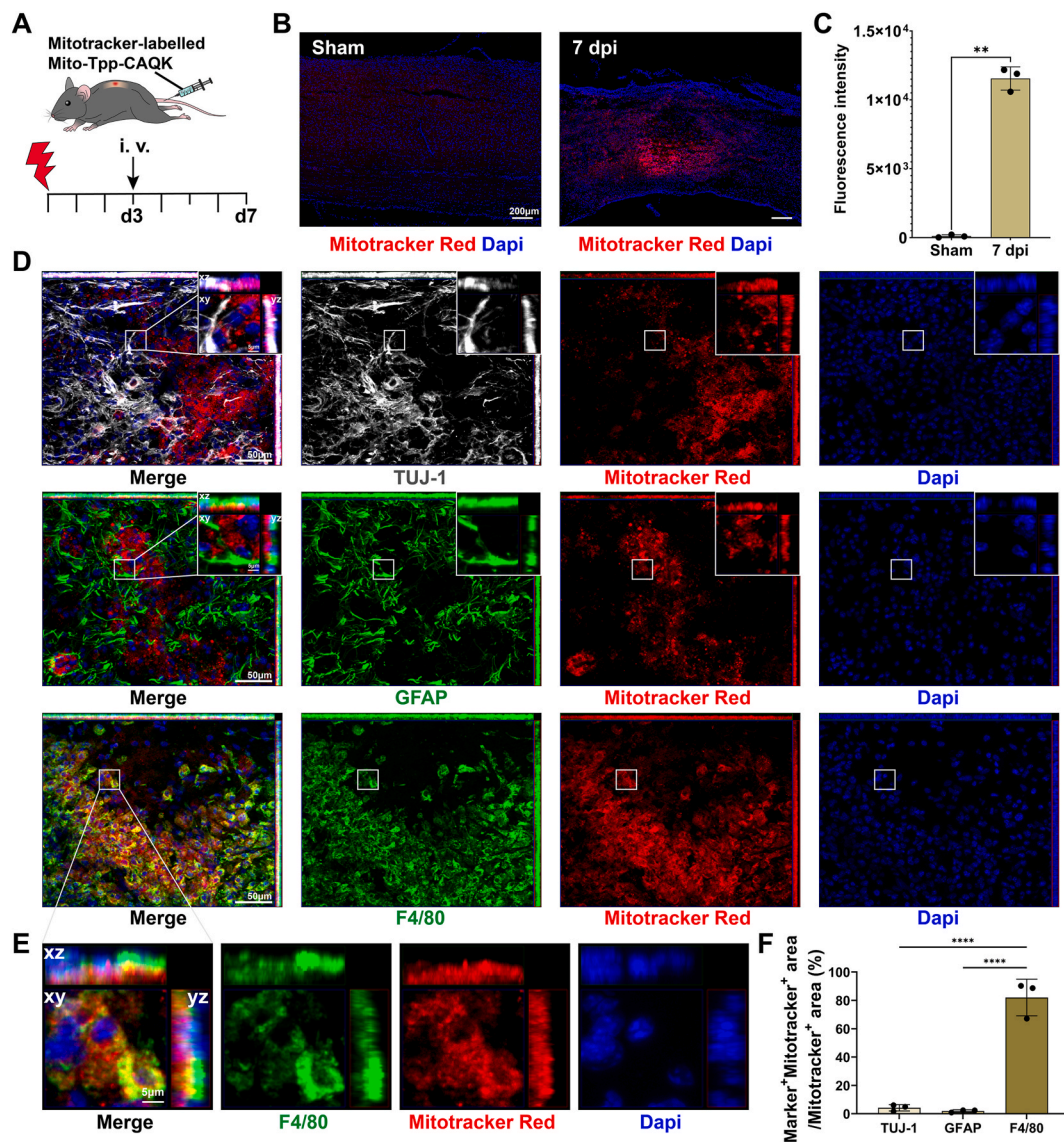

Fig. 6. The transplanted Mitochondria compounds are mainly uptake by macrophages. (A) Illustration of the process of intravenous injection of the mitotracker red-labelled Mito-Tpp-CAQK compound at day 3 after spinal cord injury. **(B)** Representative fluorescence images showing the distribution of mitotracker red after injection in the spinal cord of the sham and injury groups (red: mitotracker red, blue: DAPI, scale bar: 200 μm). **(C)** Quantification of the fluorescence intensity of mitotracker red in (B) (n = 3, mean ± SD, unpaired *t*-test, **p < 0.0). **(D)** Representative fluorescence images showing the colocalization of cell markers (TUJ-1, GFAP, F4/80) with mitotracker red in the spinal cord at 7 days post injury (dpi) (white: TUJ-1, green: GFAP/F4/80, red: mitotracker red, blue: DAPI, scale bar = 50 μm). **(E)** Localized enlargements of double immunofluorescence staining of F4/80 and mitotracker red from (D) (scale bar = 5 μm). **(F)** Quantification of the marker⁺mitotracker⁺ area/mitotracker⁺ area in (D) (n = 3, mean ± SD, one-way ANOVA, Tukey's multiple comparisons, ****p < 0.0001).

intravenous-transplanted engineered mitochondria compounds are mainly taken up by macrophages and retain their activity within these cells.

3.7. Mito-Tpp-CAQK enhanced phagocytosis of myelin debris by macrophages in vivo

We further investigate the impact of the injection of Mito-Tpp-CAQK compound on the phagocytosis of macrophages *in vivo*. We performed two mitochondrial intravenous injections on SCI mice on 3 and 5 dpi. MBP and F4/80 double immunofluorescence staining showed that in the sham group, MBP formed continuous myelin sheath structures without fragmentation near the central canal (CC), and the number of F480-positive cells was minimal (Fig. 7A). However, on 7 dpi, macrophages infiltrated the injury site, and MBP staining showed scattered myelin debris in the injury area, some of which were engulfed by macrophages. Compared with the control group, mice treated with Mito-Tpp-CAQK compound showed a significant increase in the area of MBP-positive myelin debris within macrophages (Fig. 7A and B). Localization

enlargement of three-dimensional images showed that only a small portion of myelin debris was engulfed in the cytoplasm of macrophages. However, after transplantation with the Mito-Tpp-CAQK compound, a significantly increased number of myelin debris was internalized into the cytoplasm of macrophages (Fig. 7C). The enhancement of macrophage phagocytic ability during the acute phase of spinal cord injury can have an impact on the lipids deposition within the affected area during the chronic phase. Hence, at 28 dpi, we conducted Oil Red O staining and found that the lipid deposition in the injured epicenter treated with Mito-Tpp-CAQK compound was significantly reduced as compared to the control group (Fig. 7D and E).

3.8. Mito-Tpp-CAQK alleviated the mitochondrial dysfunction and pro-inflammatory profile of macrophages after spinal cord injury

As the primary immune cells in the epicenter of spinal cord injury, the phenotype of macrophages plays a critical role in shaping the local microenvironment. Consequently, we conducted further investigations to confirm the impact of the Mito-Tpp-CAQK compound on macrophage
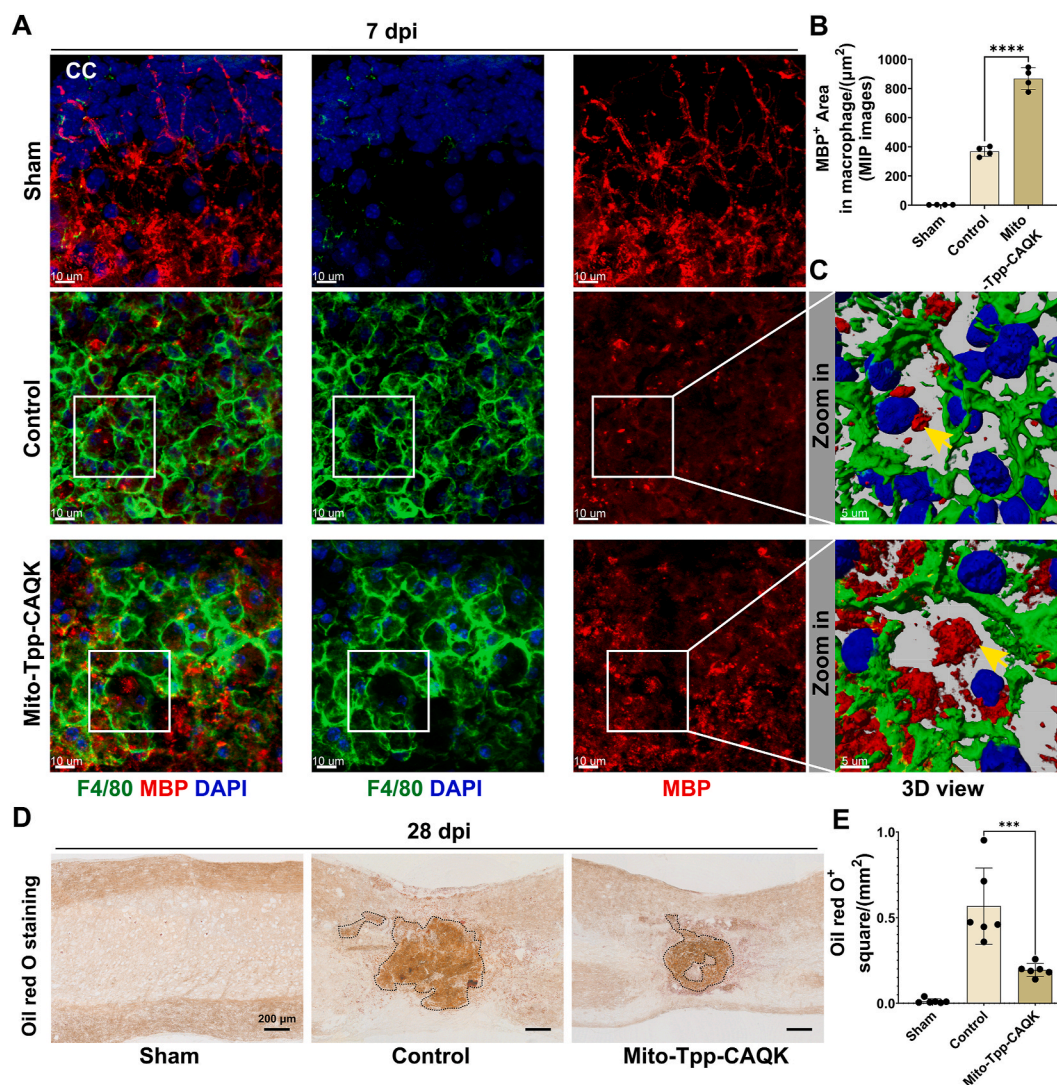

Fig. 7. **Mito-Tpp-CAQK enhanced phagocytosis of myelin debris by macrophages in vivo.** **(A)** Representative confocal images showing the double immunofluorescence staining of F4/80 and MBP in the epicenter of injured spinal cord at 7 dpi, in the sham, control, and Mito-Tpp-CAQK treated groups (green: F4/80, red: MBP, blue: DAPI, scale bar = 10 μm, CC: central canal). **(B)** Quantification of the MBP$^+$ area in F4/80 labelled macrophages in (A) (n = 4, mean ± SD, one-way ANOVA, Tukey's multiple comparisons, ****$p < 0.0001$, MIP: maximal intensity projection). **(C)** Localized enlargements of fluorescence images from (A) (scale bar = 5 μm). **(D)** Oil red O staining showing the lipid deposition of the spinal cord at 28 dpi in the sham, control, and Mito-Tpp-CAQK treated groups. **(E)** Quantification of the Oil red O area in (D) (n = 6, mean ± SD, one-way ANOVA, Tukey's multiple comparisons, ***$p < 0.001$).

mitochondrial dysfunction and pro-inflammatory profile *in vivo*. Mitochondrial TEM images revealed that in the sham group, mitochondrial morphology was normal with high matrix density and clear cristae structure. Within the injury epicenter on 14 dpi, mitochondria exhibited shrinkage, with a broken structure of the cristae, and vacuolization. In the treatment group, the structure of the mitochondrial cristae recovered, and the volume of the mitochondria in the cells significantly increased (Fig. 8A and B). Lipid peroxidation is also a manifestation of mitochondrial dysfunction. 4-HNE is a lipid peroxidation product [41].

Double immunofluorescence staining of F4/80 and 4-HNE showed that 4-HNE was generated in macrophages, while Mito-Tpp-CAQK significantly reduced the production of 4-HNE and lipid peroxidation (Fig. 8C and D). Double immunofluorescence staining of F4/80 and macrophage polarization markers showed that the Mito-Tpp-CAQK compound treatment led to a significant decrease in the expression of the M1 macrophage marker iNOS (Fig. 8E and F). Conversely, we also observed a notable increase in the expression of the anti-inflammatory marker Arg1 in F4/80-labelled macrophages (Fig. 8G and H). In light of these
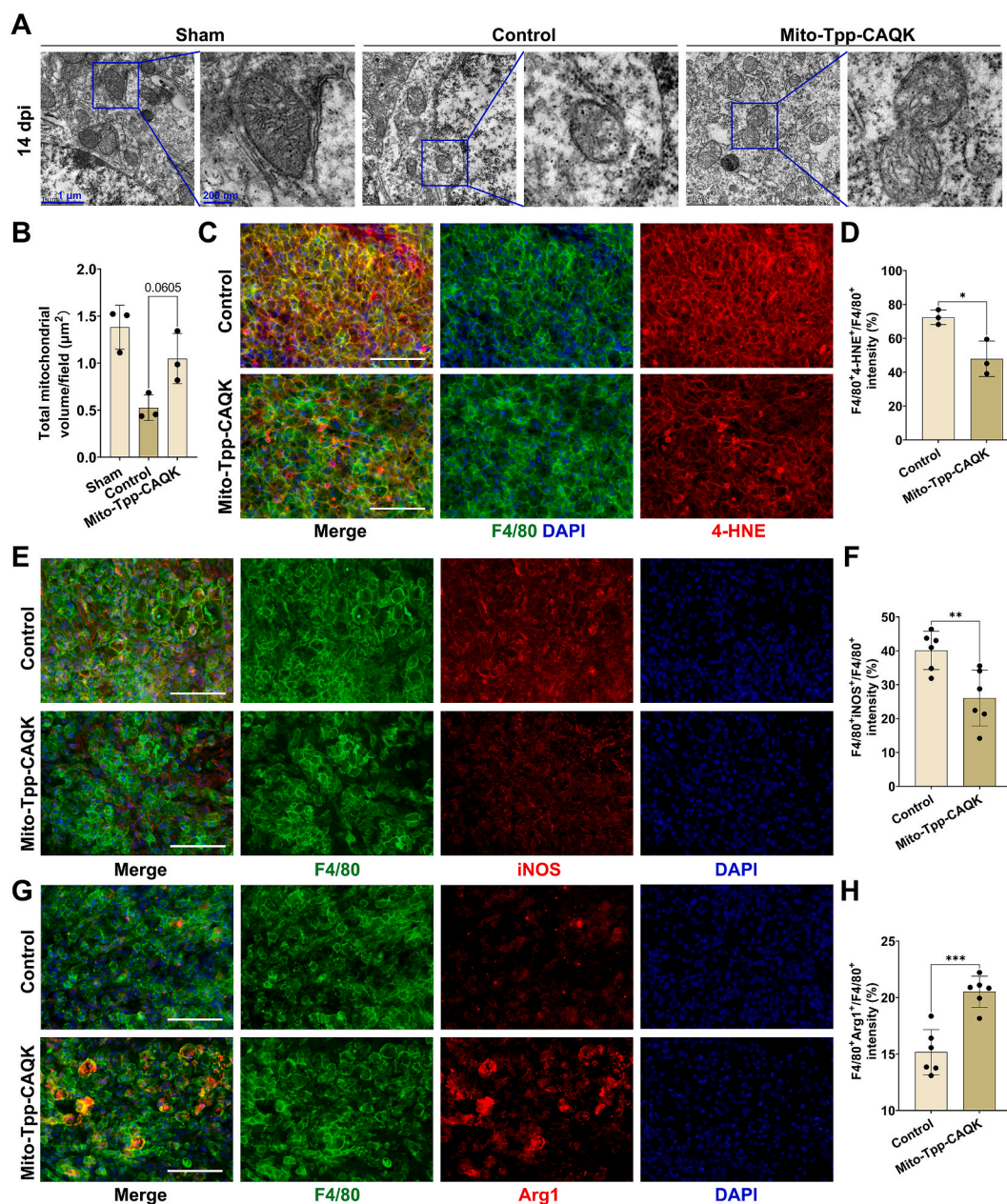

Fig. 8. Mito-Tpp-CAQK alleviated the mitochondrial dysfunction and pro-inflammatory profile of macrophages after spinal cord injury.
(A) Representative Transmission Electron Microscope (TEM) images of mitochondria morphology in the sham, control, and Mito-Tpp-CAQK treated groups.
(Scale bar = 1 μm/200 nm) **(B)** Quantification of the total mitochondrial volume per field in (A) (n = E, mean ± SD, one-way ANOVA, Tukey's multiple comparisons, p-value indicated in the figure). **(C)** Representative fluorescence images showing the double immunofluorescence staining of F4/80 and 4-HNE at 14 dpi in the control and Mito-Tpp-CAQK treated groups (green: F4/80, red: 4-HNE, blue: DAPI, scale bar = 200 μm). **(D)** Quantification of the $F4/80^+4\text{-}HNE^+/F4/80^+$ intensity in (C) (n = 3, mean ± SD, unpaired *t*-test, *p < 0.05). **(E)** Representative fluorescence images showing the double immunofluorescence staining of F4/80 and iNOS at 14 dpi in the control and Mito-Tpp-CAQK treated groups (green: F4/80, red: iNOS, scale bar = 200 μm). **(F)** Quantification of the $F4/80^+iNOS^+/F4/80^+$ intensity in (E) (n = 6, mean ± SD, unpaired *t*-test, **p < 0.01). **(G)** Representative fluorescence images showing the double immunofluorescence staining of F4/80 and Arg1 at 14 dpi in the control and Mito-Tpp-CAQK treated groups (green: F4/80, red: Arg1, scale bar = 200 μm). **(H)** Quantification of the $F4/80^+Arg1^+/F4/80^+$ intensity in (G) (n = 6, mean ± SD, unpaired *t*-test, ***p < 0.001).

findings, it can be concluded that the intravenous transplantation of the Mito-Tpp-CAQK compound alleviated the mitochondrial dysfunction of macrophages and promoted the transition of macrophages in the injury area towards a tissue repair phenotype in mice with SCI.

3.9. Mito-Tpp-CAQK promoted tissue repair and functional recovery after spinal cord injury

After confirming the effects of Mito-Tpp-CAQK on clearing myelin debris and improving the local microenvironment, we investigated whether it could further promote tissue repair and functional recovery in mice. Astrocytes, neurons, and oligodendrocytes play critical roles in
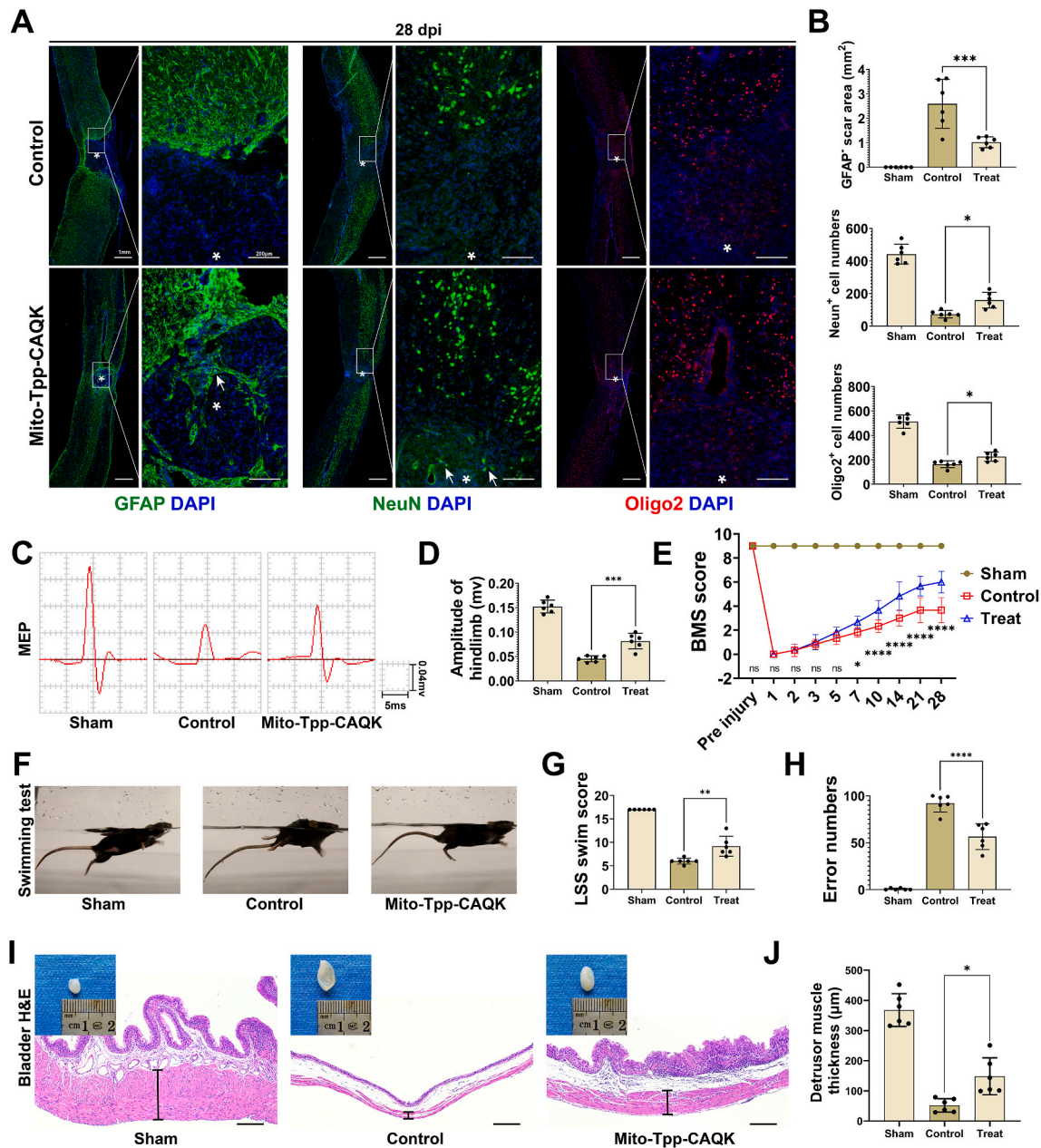

Fig. 9. Mito-Tpp-CAQK promoted tissue repair and functional recovery after spinal cord injury. **(A)** Representative fluorescence images of GFAP, NeuN, and Oligo2 of the injured spinal cord at 28 dpi in the control and Mito-Tpp-CAQK treated groups (green: GFAP/NeuN, red: Oligo2, blue: DAPI, scale bar = 1 mm/200 μm). **(B)** Quantification of the GFAP$^-$ scar area, Neun$^+$ and Oligo2$^+$ cell numbers (1.5 mm^2 area near the injured epicenter) in (A) (n = 6, mean ± SD, one-way ANOVA, Tukey's multiple comparisons, **p < 0.01 ***p < 0.001). **(C)** Representative images of hindlimb motor evoked potentials (MEPs) in the sham, control, and treatment groups at 28 dpi. **(D)** Quantification of the amplitude of hindlimb in (C) (n = 6, mean ± SD, one-way ANOVA, Tukey's multiple comparisons, ***p < 0.001). **(E)** Basso Mouse Scale (BMS) scores over time post-injury in the sham, control, and treatment groups (n = 6, mean ± SD, two-way ANOVA, Tukey's multiple comparisons, ns not significant, *p < 0.05, ****p < 0.0001). **(F)** Representative images of swimming test at 28 dpi in the sham, control, and treatment groups. **(G)** Quantification of the swimming test in (F) using the Louisville Swim Scale (LSS) swim score (n = 6, mean ± SD, one-way ANOVA, Tukey's multiple comparisons, **p < 0.01). **(H)** Quantification of the error numbers of grid walking per 100 steps at 28 dpi in the sham, control, and treatment groups (n = 6, mean ± SD, one-way ANOVA, Tukey's multiple comparisons, ****p < 0.0001). **(I)** Representative images of hematoxylin and eosin staining (H&E) of the bladder (scale bar = 200 μm) and bladder macroscopic photo at 28 dpi in the sham, control, and treatment groups. **(J)** Quantification of the detrusor muscle thickness in (I) (n = 6, mean ± SD, one-way ANOVA, Tukey's multiple comparisons, *p < 0.05).

spinal cord reconstruction. However, they are typically unable to enter the injury site and successfully rebuild the normal tissue structure after injury. Immunofluorescence images of GFAP, NeuN, and Oligo2 depicted that following the administration of Mito-Tpp-CAQK, the astrocytes migrated towards the central region of the injury site (white arrow), which significantly reduced the size of GFAP-negative scar area (Fig. 9A and B). There are a few surviving NeuN-positive neurons present in the injury site (white arrow), and the quantity of NeuN-positive neurons and Oligo2-positive oligodendrocytes surrounding the injury site considerably increased (Fig. 9A and B).

After intravenous transplantation of Mito-Tpp-CAQK, the electrophysiological testing demonstrated a significant increase in the amplitude of lower limb motor evoked potential (MEP) at 28 dpi (Fig. 9C and D). The BMS score for lower limb motor function indicated that mice in the treatment group had better recovery starting from 7 dpi. By the end of the 28 dpi, the lower limb motor function of the treated mice had significantly improved (Fig. 9E). Swimming test revealed that mice in the treatment group exhibited a more stable trunk, less inclined body angle, and reduced pendent tail, with significantly increased LSS swim scores (Fig. 9F and G). Furthermore, Mito-Tpp-CAQK treatment reduced error numbers during grid walking (Fig. 9H), suggesting improved motor coordination. Moreover, analysis of the HE slices of the mouse bladder indicated that the thickness of the detrusor muscle layer in the neurogenic bladder was significantly increased after treatment with Mito-Tpp-CAQK, which suggests the recovery of nerve innervation in the bladder (Fig. 9I and J). Collectively, our findings confirmed the positive therapeutic effect of the Mito-Tpp-CAQK compound on tissue repair and functional recovery in SCI mice.

4. Discussion

Mitochondrial transplantation consists of the process of isolation, transfer, and uptake of viable, respiration-competent mitochondria into dysfunctional cells. The transplantation can be performed either autologously or heterologously, depending on the selection of the mitochondrial source. Mitochondria contain unique intracellular machinery and mtDNA, enabling them to independently produce their own mitochondrial proteins [42]. Thus, to minimize the risk of immune rejection in the recipient, we opted to use BMDMs as the source of mitochondria in our study. This approach not only simplifies the extraction and acquisition process for clinical use, but also reduces ethical concerns and the likelihood of adverse reactions. Furthermore, as mitochondria also show heterogeneity across different cell types in the human body [43], utilizing mitochondria derived from BMDMs can enhance the targeting of macrophages in subsequent mitochondrial transplantation therapy. Obtaining mitochondria with strong functionality and high content levels is another challenge for preparing the source of mitochondria. The phenotype of macrophages is closely related to their mitochondrial function and metabolic pathways [27]. M1-polarized macrophages are typically linked with pro-inflammatory responses, due to their increased metabolic activity in glycolysis, glucose oxidation, mitochondrial respiration, and anaerobic glycolysis. In contrast, M2 macrophages are known for their association with tissue repair and anti-inflammatory responses, exhibiting increased activity in the semi-lactose pathway and mitochondrial oxidative phosphorylation [44,45]. M2 macrophages can be divided into three subtypes: M2a, M2b, and M2c. M2c macrophages are activated with IL-10 [46] and exhibit more significant local anti-inflammatory effects and more potent cell repair functions than M2 macrophages [47]. Eddie lp et al. found that IL-10 inhibits lipopolysaccharide-induced glucose uptake and glycolysis, while promoting oxidative phosphorylation. In addition, IL-10 supports the removal of dysfunctional mitochondria that exhibit low membrane potential and high levels of ROS [30]. Therefore, we pretreated macrophages with IL-10 to improve their mitochondrial functions. Moreover, IL-10-induced M2c macrophages have increased expression of Mertk [48], which is also confirmed in our flow cytometry results. Mertk is

closely related to macrophage phagocytosis and inflammatory responses [36,37]. Nicolás-Ávila et al. found that Mertk is related to mitochondrial quality control, and knocking out Mertk leads to the appearance of abnormal mitochondria and changes in metabolic status [31]. We also found that the Mertk inhibitor UNC2250 reversed the increase in mitochondrial function induced by IL-10 in macrophages. The expression of Mertk is an important indicator reflecting mitochondrial function in macrophages, and the proportion of Mertk-positive cells in macrophages induced by IL-10 is as high as 93.5%. Therefore, by utilizing IL-10-induced BMDMs with high Mertk expression, we have obtained a highly suitable donor cell for mitochondrial transplantation.

It is essential to validate the bioenergetic potential of mitochondria that are isolated in vitro and then engineered into mitochondrial compounds before performing animal experiments. We have confirmed that the in vitro isolated mitochondria display normal mitochondrial membrane potential. After treating BMDMs with mitochondrial compounds, it has been observed that the compounds can be adequately taken up by the cells and improve mitochondrial respiratory function after phagocytosis of myelin debris. This includes increased cellular energy demand at baseline, enhanced mitochondrial ATP synthesis capacity, and an elevated maximum respiratory rate achievable by the cells. Additionally, transplantation of these mitochondria has been shown to reduce ROS levels within macrophages. This indicates that the transplanted mitochondria do not contain excessive ROS products. These findings indicate the bioenergetic potential and reliability of the source of mitochondria. However, we observed that the spare respiratory capacity of the macrophages did not significantly improve, suggesting that the adaptability of cells in response to energy demand remains unchanged.

The administration method for mitochondrial transplantation should be adjusted according to the specific tissues and purposes. Traditional local mitochondrial transplantation can be performed by injecting the mitochondria in situ into the tissue using a 28 or 32 G needle. In the treatment of ischemic cardiovascular diseases, intracoronary delivery of mitochondria is also a common and effective method [10]. In neurological diseases, local injection of mitochondria is utilized in SCI [16, 17], traumatic brain injury [49], schizophrenia, Parkinson's Disease, ischemic stroke [15], and sepsis-induced brain dysfunction [24]. However, local injection of the injured spinal cord can be challenging as it requires surgical re-exposure and injection into neural tissues, which is not suitable for multiple injections. Considering these aspects, intravenous injection is a convenient and feasible option. We noted that mitochondria can be delivered to damaged tissue or organs through intravenous injection [18,50]. However, ensuring effective targeting of mitochondria to the target organs is crucial, as this can mitigate any potential adverse reactions resulting from intravenous injection and enhance the therapeutic efficacy of the treatment. CAQK is a peptide that has been shown to have the ability to specifically target extracellular matrix components (proteoglycan compound), particularly the proteoglycan compound, in the vicinity of demyelinating injuries [33, 51]. Our previous research has confirmed the deposition of chondroitin sulfate proteoglycan (CSPG) in the injured epicenter of SCI [52]. Most recently, CAQK was modified on nanoparticles or extracellular vesicles to enable targeted delivery of therapeutic agents to the site of SCI [32, 53]. On the other hand, Tpp cation is an effective mitochondrial-targeting moiety, which was used to deliver drugs to mitochondria [54,55]. By exploiting the mitochondria-binding property of Tpp, Sun et al. linked a peptide to mitochondria through Tpp and constructed a mitochondria compound to treat myocardial ischemic reperfusion injury [56]. By modifying Tpp-CAQK to mitochondria, we have designed an engineered mitochondrial compound with good biological activity. Our results of the IVIS living imaging showed that the engineered Mito-Tpp-CAQK compound could be delivered effectively to the injured area of the spinal cord and maintained a high concentration after 48 h of injection. The mitochondrial compound with targeting specificity provides a practical approach for the intravenous transplantation of mitochondria in SCI.

The success of mitochondrial transplantation ultimately hinges on the ability of the transplanted mitochondria to survive within the tissue cells. The intercellular mitochondrial transfer takes place within the spinal cord, providing a theoretical basis for the uptake and utilization of exogenous mitochondria by cells *in vivo* [57]. In our in vitro experiments, we observed that the mitotracker-red labelled Mito-Tpp-CAQK compounds were successfully taken up by macrophages, effectively reducing the toxicity of myelin debris to macrophages. Interestingly, on the fourth day after intravenous injection *in vivo*, we observed the presence of mitotracker red-labelled mitochondria within the cytoplasm of macrophages, which far exceeded the expected survival time of isolated mitochondria. This suggests that the transplanted mitochondria compounds were successfully internalized by the macrophages and were potentially functional. This is consistent with the findings of Gollihue et al., who reported that the transplanted turbo green fluorescent (tGFP)-labelled mitochondria derived from PC12 cells were mainly incorporated into OX42-positive macrophages [17].

The impact of mitochondrial compounds on macrophages' phagocytosis has two aspects. Firstly, mitochondrial compounds enhance the macrophages' capacity to phagocytose and process intracellular lipids, resulting in the timely clearance of myelin debris in the injury site and reduced lipid deposition. Secondly, mitochondrial compounds alleviate the mitochondrial dysfunction and pro-inflammatory profiles of macrophages caused by excess phagocytosing myelin debris, thereby maintaining the tissue repair capability of macrophages. After SCI, the persistently pro-inflammatory response and limited ability to promote wound healing of activated macrophages are the main causes of scar formation and obstacles to neural regeneration [25]. Myelin debris, as a potential pro-inflammatory mediator, can cause macrophages to shift towards the M1 phenotype [22]. Moreover, our data have revealed that macrophages undergo mitochondrial dysfunction associated with phagocytosis following SCI. Dysfunctional macrophages with impaired energy metabolism are trapped in the injury site and persistently produce pro-inflammatory factors, including IL-6 and IL-1β, which disrupt the microenvironmental homeostasis [58]. Mitochondrial compounds significantly enhanced macrophage phagocytosis of myelin debris both in vitro and *in vivo*, while alleviating macrophages' pro-inflammatory profiles. The increase of M2-type macrophages, marked by the expression of Arg1, indicates a phenotypic shift of macrophages towards tissue-reparative type. As a result, the reduction of myelin debris and pro-inflammatory factors has led to an improvement in the microenvironment of the injury site, ultimately increasing the survival of astrocytes, neurons, and oligodendrocytes in the area. These collectively suggest that the transplantation of mitochondria compounds has created a more conducive environment for other cells to regenerate and survive.

The evaluation of electrophysiology, lower limb motor function and bladder function in mice all show the significant potential of engineered mitochondrial compounds in the treatment of SCI. It is important to note that the practical application of mitochondrial transplantation in patients will require further research to address potential issues, including preserving mitochondrial activity, efficient extraction, and determining the appropriate dosage for treatment. The storage conditions of mitochondria were not investigated here. After a large number of active mitochondria are extracted, their vitality may decrease during long-term storage, which may affect therapeutic effects. Additionally, our research should have included further experiments to investigate the optimal dosage and frequency of mitochondrial injections in mice. We performed two injections with 2–5×10^6/ml of mitochondria in 200ul of mitochondrial storage solution at 3 dpi and 5 dpi, which is the onset and peak of pro-inflammatory macrophage infiltration [59]. Whether higher levels of mitochondria or more frequent injections will yield improved therapeutic effect requires further investigation.

5. Conclusion

To summarize, we isolated energetic mitochondria from IL-10-induced Mertk[hi] BMDMs and then constructed an engineered Mito-Tpp-CAQK compound by linking the mitochondria with Tpp-CAQK. These engineered mitochondrial compounds exhibited remarkable a remarkable ability to specifically target injury sites. We demonstrated that intravenously transplanted Mito-Tpp-CAQK compounds were mainly taken up by macrophages, leading to enhanced phagocytosis of myelin debris, a reduction in mitochondrial dysfunction, and a decrease in pro-inflammatory profiles. Consequently, the intravenous administration of Mito-Tpp-CAQK led to better tissue repair and functional recovery after SCI in mice. Overall, this therapeutic approach shows great promise for clinical applications in SCI management.

Ethical standards

All research protocols were approved by the Animal Ethics Committee of Central South University (CSU). Animal care and use during our experiment were conducted under the guidelines of the Administration Committee of Affairs Concerning Experimental Animals in Hunan Province, China.

Conflict of interest

The authors declare that they have no competing financial interests or personal relationships that could have appeared to influence the work reported in this paper.

CRediT authorship contribution statement

Jiaqi Xu: Formal analysis, Investigation, Methodology, Visualization, Writing – original draft. **Chaoran Shi:** Formal analysis, Investigation, Methodology, Visualization, Writing – original draft. **Feifei Yuan:** Investigation, Methodology, Validation. **Yinghe Ding:** Visualization, Software. **Yong Xie:** Formal analysis, Writing – review & editing. **Yudong Liu:** Formal analysis, Writing – review & editing. **Fengzhang Zhu:** Investigation, Methodology, Validation. **Hongbin Lu:** Writing – review & editing, Supervision. **Chunyue Duan:** Writing – review & editing, Supervision. **Jianzhong Hu:** Conceptualization, Data curation, Funding acquisition, Project administration, Resources, All authors had approved the manuscript. **Liyuan Jiang:** Conceptualization, Data curation, Funding acquisition, Project administration, Resources.

Appendix A. Supplementary data

Supplementary data to this article can be found online at https://doi.org/10.1016/j.bioactmat.2023.10.016.

References

[1] C.S. Ahuja, J.R. Wilson, S. Nori, M.R.N. Kotter, C. Druschel, A. Curt, M.G. Fehlings, Traumatic spinal cord injury, Nat. Rev. Dis. Prim. 3 (2017), 17018, https://doi.org/10.1038/nrdp.2017.18.

[2] W. Ding, S. Hu, P. Wang, H. Kang, R. Peng, Y. Dong, F. Li, Spinal cord injury: the global incidence, prevalence, and disability from the global burden of disease study 2019, Spine 47 (21) (2022) 1532–1540, https://doi.org/10.1097/BRS.0000000000004417.

[3] S. Hu, P. Wang, Y. Dong, F. Li, Incidence, prevalence and disability of spinal cord injury in China from 1990 to 2019: a systematic analysis of the Global Burden of Disease Study 2019, Eur. Spine J. 32 (2) (2023) 590–600, https://doi.org/10.1007/s00586-022-07441-2. Official Publication of the European Spine Society, the European Spinal Deformity Society, and the European Section of the Cervical Spine Research Society.

[4] P. Assinck, G.J. Duncan, B.J. Hilton, J.R. Plemel, W. Tetzlaff, Cell transplantation therapy for spinal cord injury, Nat. Neurosci. 20 (5) (2017) 637–647, https://doi.org/10.1038/nn.4541.

[5] W.Z. Liu, Z.J. Ma, J.R. Li, X.W. Kang, Mesenchymal stem cell-derived exosomes: therapeutic opportunities and challenges for spinal cord injury, Stem Cell Res. Ther. 12 (1) (2021) 102, https://doi.org/10.1186/s13287-021-02153-8.

[6] C.S. Ahuja, S. Nori, L. Tetreault, J. Wilson, B. Kwon, J. Harrop, D. Choi, M.G. Fehlings, Traumatic spinal cord injury-repair and regeneration, Neurosurgery 80 (3s) (2017) S9–s22, https://doi.org/10.1093/neuros/nyw080.

[7] S.A. Quadri, M. Farooqui, A. Ikram, A. Zafar, M.A. Khan, S.S. Suriya, C.F. Claus, B. Fiani, M. Rahman, A. Ramachandran, I.I.T. Armstrong, M.A. Taqi, M.M. Mortazavi, Recent update on basic mechanisms of spinal cord injury, Neurosurg. Rev. 43 (2) (2020) 425–441, https://doi.org/10.1007/s10143-018-1008-3.

[8] P.G. Slater, M.E. Domínguez-Romero, M. Villarreal, V. Eisner, J. Larraín, Mitochondrial function in spinal cord injury and regeneration, Cell. Mol. Life Sci. 79 (5) (2022) 239, https://doi.org/10.1007/s00018-022-04261-x.

[9] Q. Han, Y. Xie, J.D. Ordaz, A.J. Huh, N. Huang, W. Wu, N. Liu, K.A. Chamberlain, Z.-H. Sheng, X.-M. Xu, Restoring cellular energetics promotes axonal regeneration and functional recovery after spinal cord injury, Cell Metabol. 31 (3) (2020) 623–641, https://doi.org/10.1016/j.cmet.2020.02.002.

[10] J.D. McCully, P.J. Del Nido, S.M. Emani, Mitochondrial transplantation for organ rescue, Mitochondrion 64 (2022) 27–33, https://doi.org/10.1016/j.mito.2022.02.007.

[11] L. Margulis, Symbiotic theory of the origin of eukaryotic organelles; criteria for proof, Symp. Soc. Exp. Biol. (29) (1975) 21–38.

[12] D. Liu, Y. Gao, J. Liu, Y. Huang, J. Yin, Y. Feng, L. Shi, B.P. Meloni, C. Zhang, M. Zheng, J. Gao, Intercellular mitochondrial transfer as a means of tissue revitalization, Signal Transduct. Targeted Ther. 6 (1) (2021) 65, https://doi.org/10.1038/s41392-020-00440-z.

[13] A. Park, M. Oh, S.J. Lee, K.J. Oh, E.W. Lee, S.C. Lee, K.H. Bae, B.S. Han, W.K. Kim, Mitochondrial transplantation as a novel therapeutic strategy for mitochondrial diseases, Int. J. Mol. Sci. 22 (9) (2021), https://doi.org/10.3390/ijms22094793.

[14] J.C. Chang, H.S. Chang, Y.C. Wu, W.L. Cheng, T.T. Lin, H.J. Chang, S.J. Kuo, S.T. Chen, C.S. Liu, Mitochondrial transplantation regulates antitumour activity, chemoresistance and mitochondrial dynamics in breast cancer, J. Exp. Clin. Cancer Res. 38 (1) (2019) 30, https://doi.org/10.1186/s13046-019-1028-z.

[15] Y. Nakamura, J.-H. Park, K. Hayakawa, Therapeutic use of extracellular mitochondria in CNS injury and disease, Exp. Neurol. 324 (2020) 113114, https://doi.org/10.1016/j.expneurol.2019.113114.

[16] M.W. Lin, S.Y. Fang, J.C. Hsu, C.Y. Huang, P.H. Lee, C.C. Huang, H.F. Chen, C.F. Lam, J.S. Lee, Mitochondrial transplantation attenuates neural damage and improves locomotor function after traumatic spinal cord injury in rats, Front. Neurosci. 16 (2022), 800883, https://doi.org/10.3389/fnins.2022.800883.

[17] J.L. Gollihue, S.P. Patel, K.C. Eldahan, D.H. Cox, R.R. Donahue, B.K. Taylor, P.G. Sullivan, A.G. Rabchevsky, Effects of mitochondrial transplantation on bioenergetics, cellular incorporation, and functional recovery after spinal cord injury, J. Neurotrauma 35 (15) (2018) 1800–1818, https://doi.org/10.1089/neu.2017.5605.

[18] S.Y. Fang, J.N. Roan, J.S. Lee, M.H. Chiu, M.W. Lin, C.C. Liu, C.F. Lam, Transplantation of viable mitochondria attenuates neurologic injury after spinal cord ischemia, J. Thorac. Cardiovasc. Surg. 161 (5) (2021) e337–e347, https://doi.org/10.1016/j.jtcvs.2019.10.151.

[19] S.P. Patel, F.M. Michael, M. Arif Khan, B. Duggan, S. Wyse, D.R. Darby, K. Chaudhuri, J.T. Pham, J.E. DeRouchey, P.G. Sullivan, T.D. Dziubla, A.G. Rabchevsky, Erodible thermogelling hydrogels for localized mitochondrial transplantation to the spinal cord, Mitochondrion 64 (2022) 145–155, https://doi.org/10.1016/j.mito.2022.04.002.

[20] J. Van Broeckhoven, D. Sommer, D. Dooley, S. Hendrix, A.J.P.M. Franssen, Macrophage phagocytosis after spinal cord injury: when friends become foes, Brain 144 (10) (2021) 2933–2945, https://doi.org/10.1093/brain/awab250.

[21] X. Sheng, J. Zhao, M. Li, Y. Xu, Y. Zhou, J. Xu, R. He, H. Lu, T. Wu, C. Duan, Y. Cao, J. Hu, Bone marrow mesenchymal stem cell-derived exosomes accelerate functional recovery after spinal cord injury by promoting the phagocytosis of macrophages to clean myelin debris, Front. Cell Dev. Biol. 9 (2021), 772205, https://doi.org/10.3389/fcell.2021.772205.

[22] T.J. Kopper, J.C. Gensel, Myelin as an inflammatory mediator: myelin interactions with complement, macrophages, and microglia in spinal cord injury, J. Neurosci. Res. 96 (6) (2018) 969–977, https://doi.org/10.1002/jnr.24114.

[23] C.B. Ryan, J.S. Choi, H. Al-Ali, J.K. Lee, Myelin and non-myelin debris contribute to foamy macrophage formation after spinal cord injury, Neurobiol. Dis. 163 (2022), 105608, https://doi.org/10.1016/j.nbd.2021.105608.

[24] C. Yan, Z. Ma, H. Ma, Q. Li, Q. Zhai, T. Jiang, Z. Zhang, Q. Wang, Mitochondrial transplantation attenuates brain dysfunction in sepsis by driving microglial M2 polarization, Mol. Neurobiol. 57 (9) (2020) 3875–3890, https://doi.org/10.1007/s12035-020-01994-3.

[25] J.C. Gensel, B. Zhang, Macrophage activation and its role in repair and pathology after spinal cord injury, Brain Res. 1619 (2015) 1–11, https://doi.org/10.1016/j.brainres.2014.12.045.

[26] S. Nair, K.S. Sobotka, P. Joshi, P. Gressens, B. Fleiss, C. Thornton, C. Mallard, H. Hagberg, Lipopolysaccharide-induced alteration of mitochondrial morphology induces a metabolic shift in microglia modulating the inflammatory response in vitro and in vivo, Glia 67 (6) (2019) 1047–1061, https://doi.org/10.1002/glia.23587.

[27] J. Van den Bossche, L.A. O'Neill, D. Menon, Macrophage immunometabolism: where are we (going)? Trends Immunol. 38 (6) (2017) 395–406, https://doi.org/10.1016/j.it.2017.03.001.

[28] Y. Wang, N. Li, X. Zhang, T. Horng, Mitochondrial metabolism regulates macrophage biology, J. Biol. Chem. 297 (1) (2021), 100904, https://doi.org/10.1016/j.jbc.2021.100904.

[29] S.K. Wculek, I. Heras-Murillo, A. Mastrangelo, D. Mañanes, M. Galán, V. Miguel, A. Curtabbi, C. Barbas, N.S. Chandel, J.A. Enríquez, S. Lamas, D. Sancho, Oxidative phosphorylation selectively orchestrates tissue macrophage homeostasis, Immunity 56 (3) (2023) 516–530.e9, https://doi.org/10.1016/j.immuni.2023.01.011.

[30] W.K.E. Ip, N. Hoshi, D.S. Shouval, S. Snapper, R. Medzhitov, Anti-inflammatory effect of IL-10 mediated by metabolic reprogramming of macrophages, Science 356 (6337) (2017) 513–519, https://doi.org/10.1126/science.aal3535.

[31] J.A. Nicolás-Ávila, A.V. Lechuga-Vieco, L. Esteban-Martínez, M. Sánchez-Díaz, E. Díaz-García, D.J. Santiago, A. Rubio-Ponce, J.L. Li, A. Balachander, J.A. Quintana, R. Martínez-de-Mena, B. Castejón-Vega, A. Pun-García, P.G. Través, E. Bonzón-Kulichenko, F. García-Marqués, L. Cussó, A.G. N, A. González-Guerra, M. Roche-Molina, S. Martin-Salamanca, G. Crainiciuc, G. Guzmán, J. Larrazabal, E. Herrero-Galán, J. Alegre-Cebollada, G. Lemke, C.V. Rothlin, L.J. Jimenez-Borreguero, G. Reyes, A. Castrillo, M. Desco, P. Muñoz-Cánoves, B. Ibáñez, M. Torres, L.G. Ng, S.G. Priori, H. Bueno, J. Vázquez, M.D. Cordero, J.A. Bernal, J.A. Enríquez, A. Hidalgo, A network of macrophages supports mitochondrial homeostasis in the heart, Cell 183 (1) (2020) 94–109.e23, https://doi.org/10.1016/j.cell.2020.08.031.

[32] Y. Rong, Z. Wang, P. Tang, J. Wang, C. Ji, J. Chang, Y. Zhu, W. Ye, J. Bai, W. Liu, G. Yin, L. Yu, X. Zhou, W. Cai, Engineered extracellular vesicles for delivery of siRNA promoting targeted repair of traumatic spinal cord injury, Bioact. Mater. 23 (2023) 328–342, https://doi.org/10.1016/j.bioactmat.2022.11.011.

[33] A.P. Mann, P. Scodeller, S. Hussain, J. Joo, E. Kwon, G.B. Braun, T. Mölder, Z.G. She, V.R. Kotamraju, B. Ranscht, S. Krajewski, T. Teesalu, S. Bhatia, M.J. Sailor, E. Ruoslahti, A peptide for targeted, systemic delivery of imaging and therapeutic compounds into acute brain injuries, Nat. Commun. 7 (2016), 11980, https://doi.org/10.1038/ncomms11980.

[34] R. Satija, J.A. Farrell, D. Gennert, A.F. Schier, A. Regev, Spatial reconstruction of single-cell gene expression data, Nat. Biotechnol. 33 (5) (2015) 495–502, https://doi.org/10.1038/nbt.3192.

[35] E. Grajchen, E. Wouters, B. van de Haterd, M. Haidar, K. Hardonnière, T. Dierckx, J. Van Broeckhoven, C. Erens, S. Hendrix, S. Kerdine-Römer, J.J.A. Hendriks, J.F.J. Bogie, CD36-mediated uptake of myelin debris by macrophages and microglia reduces neuroinflammation, J. Neuroinflammation 17 (1) (2020) 224, https://doi.org/10.1186/s12974-020-01899-x.

[36] J.H. Park, J.H. Kim, S.-K. Oh, S.R. Baek, J. Min, Y.W. Kim, S.T. Kim, C.-W. Woo, S.R. Jeon, Analysis of equivalent parameters of two spinal cord injury devices: the New York University impactor versus the Infinite Horizon impactor, Spine J.: Off. J. North Am. Spine Soc. 16 (11) (2016) 1392–1403, https://doi.org/10.1016/j.spinee.2016.06.018.

[37] D.M. Basso, L.C. Fisher, A.J. Anderson, L.B. Jakeman, D.M. McTigue, P.G. Popovich, Basso Mouse Scale for locomotion detects differences in recovery after spinal cord injury in five common mouse strains, J. Neurotrauma 23 (5) (2006) 635–659.

[38] R.R. Smith, D.A. Burke, A.D. Baldini, A. Shum-Siu, R. Baltzley, M. Bunger, D.S. Magnuson, The Louisville Swim Scale: a novel assessment of hindlimb function following spinal cord injury in adult rats, J. Neurotrauma 23 (11) (2006) 1654–1670, https://doi.org/10.1089/neu.2006.23.1654.

[39] Y. Liu, L. Lan, Y. Li, J. Lu, L. He, Y. Deng, M. Fei, J.W. Lu, F. Shangguan, J.P. Lu, J. Wang, L. Wu, K. Huang, B. Lu, N-glycosylation stabilizes MerTK and promotes hepatocellular carcinoma tumor growth, Redox Biol. 54 (2022), 102366, https://doi.org/10.1016/j.redox.2022.102366.

[40] L.M. Healy, J.H. Jang, S.Y. Won, Y.H. Lin, S. Touil, S. Aljarallah, A. Bar-Or, J.P. Antel, MerTK-mediated regulation of myelin phagocytosis by macrophages generated from patients with MS, Neurol. Neuroimmunol. Neuroinflamm. 4 (6) (2017), e402, https://doi.org/10.1212/nxi.0000000000000402.

[41] J. Xu, Y. Ding, C. Shi, F. Yuan, X. Sheng, Y. Liu, Y. Xie, H. Lu, C. Duan, J. Hu, L. Jiang, Identification of Cathepsin B as a Therapeutic Target for Ferroptosis of Macrophage after Spinal Cord Injury, Aging and Disease, Online ahead of print, https://doi.org/10.14336/ad.2023.0509, 2023.

[42] J.M. Shaw, D.R. Winge, Shaping the mitochondrion: mitochondrial biogenesis, dynamics and dysfunction. Conference on mitochondrial assembly and dynamics in health and disease, EMBO Rep. 10 (12) (2009) 1301–1305, https://doi.org/10.1038/embor.2009.247.

[43] J.B. Stewart, P.F. Chinnery, The dynamics of mitochondrial DNA heteroplasmy: implications for human health and disease, Nat. Rev. Genet. 16 (9) (2015) 530–542, https://doi.org/10.1038/nrg3966.

[44] J. Van den Bossche, J. Baardman, M.P. de Winther, Metabolic characterization of polarized M1 and M2 bone marrow-derived macrophages using real-time extracellular Flux analysis, J. Vis. Exp. 105 (2015) 53424, https://doi.org/10.3791/53424.

[45] J. Van den Bossche, J. Baardman, N.A. Otto, S. van der Velden, A.E. Neele, S. M. van den Berg, R. Luque-Martin, H.J. Chen, M.C. Boshuizen, M. Ahmed, M. A. Hoeksema, A.F. de Vos, M.P. de Winther, Mitochondrial dysfunction prevents repolarization of inflammatory macrophages, Cell Rep. 17 (3) (2016) 684–696, https://doi.org/10.1016/j.celrep.2016.09.008.

[46] X. Huang, Y. Li, M. Fu, H.B. Xin, Polarizing macrophages in vitro, Methods Mol. Biol. 1784 (2018) 119–126, https://doi.org/10.1007/978-1-4939-7837-3_12.

[47] E.B. Lurier, D. Dalton, W. Dampier, P. Raman, S. Nassiri, N.M. Ferraro, R. Rajagopalan, M. Sarmady, K.L. Spiller, Transcriptome analysis of IL-10-stimulated (M2c) macrophages by next-generation sequencing, Immunobiology 222 (7) (2017) 847–856, https://doi.org/10.1016/j.imbio.2017.02.006.

[48] Junior, Y.S. Lai, H.T. Nguyen, F.P. Salmanida, K.T. Chang, MERTK(+/hi) M2c macrophages induced by baicalin alleviate non-alcoholic fatty liver disease, Int. J. Mol. Sci. 22 (19) (2021), https://doi.org/10.3390/ijms221910604.

[49] J. Zhao, D. Qu, Z. Xi, Y. Huan, K. Zhang, C. Yu, D. Yang, J. Kang, W. Lin, S. Wu, Y. Wang, Mitochondria transplantation protects traumatic brain injury via promoting neuronal survival and astrocytic BDNF, Transl. Res. 235 (2021) 102–114, https://doi.org/10.1016/j.trsl.2021.03.017.

[50] X. Shi, M. Zhao, C. Fu, A. Fu, Intravenous administration of mitochondria for treating experimental Parkinson's disease, Mitochondrion 34 (2017) 91–100, https://doi.org/10.1016/j.mito.2017.02.005.

[51] C. Abi-Ghanem, D. Jonnalagadda, J. Chun, Y. Kihara, B. Rancht, CAQK, a peptide associating with extracellular matrix components targets sites of demyelinating injuries, Front. Cell. Neurosci. 16 (2022), 908401, https://doi.org/10.3389/fncel.2022.908401.

[52] C. Li, T. Qin, J. Zhao, R. He, H. Wen, C. Duan, H. Lu, Y. Cao, J. Hu, Bone marrow mesenchymal stem cell-derived exosome-educated macrophages promote functional healing after spinal cord injury, Front. Cell. Neurosci. 15 (2021), 725573, https://doi.org/10.3389/fncel.2021.725573.

[53] T. Li, P. Jing, L. Yang, Y. Wan, X. Du, J. Wei, M. Zhou, Z. Liu, Y. Lin, Z. Zhong, CAQK modification enhances the targeted accumulation of metformin-loaded nanoparticles in rats with spinal cord injury, Nanomedicine 41 (2022), 102526, https://doi.org/10.1016/j.nano.2022.102526.

[54] G. Cheng, J. Zielonka, O. Ouari, M. Lopez, D. McAllister, K. Boyle, C.S. Barrios, J. J. Weber, B.D. Johnson, M. Hardy, M.B. Dwinell, B. Kalyanaraman, Mitochondria-targeted analogues of metformin exhibit enhanced antiproliferative and radiosensitizing effects in pancreatic cancer cells, Cancer Res. 76 (13) (2016) 3904–3915, https://doi.org/10.1158/0008-5472.Can-15-2534.

[55] J. Zielonka, J. Joseph, A. Sikora, M. Hardy, O. Ouari, J. Vasquez-Vivar, G. Cheng, M. Lopez, B. Kalyanaraman, Mitochondria-targeted triphenylphosphonium-based compounds: syntheses, mechanisms of action, and therapeutic and diagnostic applications, Chem. Rev. 117 (15) (2017) 10043–10120, https://doi.org/10.1021/acs.chemrev.7b00042.

[56] X. Sun, H. Chen, R. Gao, Y. Qu, Y. Huang, N. Zhang, S. Hu, F. Fan, Y. Zou, K. Hu, Z. Chen, J. Ge, A. Sun, Intravenous transplantation of an ischemic-specific peptide-TPP-mitochondrial compound alleviates myocardial ischemic reperfusion injury, ACS Nano 17 (2) (2023) 896–909, https://doi.org/10.1021/acsnano.2c05286.

[57] H. Li, C. Wang, T. He, T. Zhao, Y.Y. Chen, Y.L. Shen, X. Zhang, L.L. Wang, Mitochondrial transfer from bone marrow mesenchymal stem cells to motor neurons in spinal cord injury rats via gap junction, Theranostics 9 (7) (2019) 2017–2035, https://doi.org/10.7150/thno.29400.

[58] D.J. Hellenbrand, C.M. Quinn, Z.J. Piper, C.N. Morehouse, J.A. Fixel, A.S. Hanna, Inflammation after spinal cord injury: a review of the critical timeline of signaling cues and cellular infiltration, J. Neuroinflammation 18 (1) (2021) 284, https://doi.org/10.1186/s12974-021-02337-2.

[59] L.M. Milich, C.B. Ryan, J.K. Lee, The origin, fate, and contribution of macrophages to spinal cord injury pathology, Acta Neuropathol. 137 (5) (2019) 785–797, https://doi.org/10.1007/s00401-019-01992-3.